Revista Mexicana de Astronomía y Astrofísica, **42**, 53–74 (2006)

GALACTIC PLANETARY NEBULAE WITH WOLF-RAYET NUCLEI III. KINEMATICAL ANALYSIS OF A LARGE SAMPLE OF NEBULAE[1]

S. Medina,[2] M. Peña,[2] C. Morisset,[2] and G. Stasińska[3]

Received 2005 August 8; accepted 2005 December 6

RESUMEN

Se midieron y analizaron las velocidades de expansión ($V_{\rm exp}$) de diferentes iones y el ancho en la base de las líneas en 24 nebulosas planetarias (NPs) con núcleo [WC] (WRPNe), 9 NPs ionizadas por WELS (WLPNe) y 14 NPs normales. El estudio comparativo del comportamiento cinemático de los objetos muestra que las WRPNe tienen $V_{\rm exp}$ 40–45% mayores y más turbulencia que las WLPNe y PNe normales. Las WLPNe tienen comportamiento cinemático muy similar a las NPs normales. Todos los objetos muestran $V_{\rm exp}$ que aumenta con los indicadores de edad (densidad nebular y temperatura de las estrellas), pero el efecto es mayor en las WRPNe evolucionadas, sugiriendo que el intenso viento estelar ha acelerado a la nebulosa por largo tiempo. En los objetos no-WR, la aceleración de la nebulosa se detiene cuando la estrella alcanza una temperatura del orden de 90,000 – 100,000 K y $V_{\rm exp}$ llega a un valor máximo de 30 km s^{-1}. Las WRPNe alcanzan $V_{\rm exp}$ máximas del orden de 40 km s^{-1}. Encontramos que $V_{\rm exp}(N^+)$ es ligeramente mayor que $V_{\rm exp}(O^{++})$ en todo tipo de objetos, indicando que las nebulosas muestran aceleración en las capas externas.

ABSTRACT

Expansion velocities ($V_{\rm exp}$) of different ions and line widths at the base of the lines are measured and analyzed for 24 PNe with [WC]-type nuclei (WRPNe), 9 PNe ionized by WELS (WLPNe) and 14 ordinary PNe. A comparative study of the kinematical behavior of the sample clearly demonstrates that WRPNe have on average 40–45% larger $V_{\rm exp}$, and possibly more turbulence than WLPNe and ordinary PNe. WLPNe have velocity fields very much like the ones of ordinary PNe, rather than the ones of WRPNe. All the samples (WRPNe, WLPNe and ordinary PNe) show expansion velocities increasing with age indicators, for example $<V_{\rm exp}>$ is larger for low-density nebulae and also it is larger for nebulae around high-temperature stars. This age effect is much stronger for evolved WRPNe, suggesting that the [WC] winds have been accelerating the nebulae for a long time, while for non-WRPNe the acceleration seems to stop at some point when the star reaches a temperature of about 90,000 – 100,000 K. Non-WR nebulae reach a maximum $V_{\rm exp} \leq 30$ km s^{-1} while evolved WRPNe reach maximum $V_{\rm exp}$ of about 40 km s^{-1}. For all kinds of objects (WRPNe and non-WRPNe) it is found that on average $V_{\rm exp}(N^+)$ is slightly larger than $V_{\rm exp}(O^{++})$, indicating that the nebulae present acceleration of the external shells.

Key Words: **PLANETARY NEBULAE: INDIVIDUAL: NGC 6369, M 1-32, BD+30°3639, K 2-16 — STARS: WOLF-RAYET**

[1]Based on data collected at the Observatorio Astronómico Nacional, San Pedro Mártir, B. C., México.

[2]Instituto de Astronomía, Universidad Nacional Autónoma de México, México.
[3]LUTH, Observatoire de Meudon, France.

1. INTRODUCTION

Among galactic planetary nebulae with known central stars, less than 15% have nuclei presenting Wolf-Rayet features. All these stars have been classified as belonging to the [WC] spectral type, showing almost pure helium and carbon in their atmospheres (e.g., Tylenda, Acker, & Stenholm 1993; Hamann 1997). The only possible [WN] central star in the Galaxy was reported by Morgan, Parker, & Cohen (2003).

Many recent studies have been devoted to these planetary nebulae (hereinafter WRPNe) and their central stars with interesting new results. Górny & Stasińska (1995) found that the physical properties and chemical abundances of WRPNe were not different from those of non-WRPNe, except for higher expansion velocities. Since then, Peña et al.(1998, Paper I) found that central stars of different initial masses can pass through the same [WC] stage and Peña, Stasińska, & Medina (2001, Paper II) reported an unexpected behavior of the [O III]/[N II] electron temperature ratios for WRPNe which does not seem to be present in non-WRPNe. In addition, Górny et al. (2001) have found that in an infrared diagram (H–K) versus (J–H), WRPNe spread over a larger zone than non-WRPNe which is probably more reflecting differences in dust and stellar properties rather than differences in nebular properties. Acker et al. (2002) have concluded that WRPNe show similar expansion velocities but larger turbulent velocities that normal PNe, and recently Gesicki, Acker, & Zijlstra (2003) concluded that the WRPNe tend to show strong acceleration at the ionization front and strong turbulent motions.

For the central stars, several scenarios to produce such H-deficient low-mass stars have been proposed (e.g., Blöcker 2001; Herwig 2001). In addition, Górny & Tylenda (2000) and De Marco (2002) have provided further arguments for the existence of the evolutionary sequence: [WC]-late $\rightarrow$ [WC]-early stars, ending with the PG 1159 type stars, proposed by Acker, Gorny, & Cuisinier (1996) and Hamann (1997). However, this proposition is still being debated (Hamann, Todt & Grafener 2005).

Parthasarathy, Acker, & Stenholm (1998) have claimed that "weak emission line stars" (WELS), as defined by Tylenda et al. (1993), are an intermediate stage between [WC] and PG 1159 stars. However, Peña et al. (2001) have argued that PNe around WELS are more similar to ordinary PNe than to WRPNe and consider doubtful the proposition of Parthasarathy et al.

Between 1995 and 2000, we have performed systematic observations of WRPNe, to gather a homogeneous high-resolution spectroscopic data set for studying the nature and evolutionary status of WRPNe. From these data, in Paper I we presented detailed photoionization models for a sample of very high excitation nebulae ionized by [WC 2-3] central stars, and in Paper II we reported line intensities, physical conditions and chemical composition for 34 PNe with nuclei of all [WC] spectral types, including a few WELS.

In this work, our high resolution data are employed to analyze the kinematical behaviour of 24 WRPNe (most of them presented in Paper II) with the purpose of studying the effects of the powerful [WC] winds on the nebular shells. We analyze some phenomena affecting the nebular profiles such as expansion velocities, turbulence and high velocity material. In particular we address the problem of whether WRPNe present higher expansion velocities and/or turbulence than non-WRPNe. To perform our analysis we have included a sample of 14 ordinary planetary nebulae (i.e., whose nuclei are neither WR nor WELS) which are useful as a control sample to confirm that any special trend found for WRPNe is not an instrumental effect. Nine PNe ionized by a WELS (hereinafter WLPNe) have been included also in the analysis.

In § 2, the observations and data reduction are described. The line profiles are discussed in § 3. The expansion velocities derived for the sample are presented and analyzed in § 4, where a brief discussion regarding turbulence can be found. In § 5, we present the line widths at the base of lines, searching for the highest velocity material. The kinematical analysis of selected nebular lines is presented in § 6. Our main conclusions are summarized in § 7. Finally, two Appendices have been included, where we present some examples of our data and discuss some objects with particularly interesting profiles or kinematics.

2. OBSERVATIONS AND DATA REDUCTION

High-resolution spectroscopic data were systematically gathered with the 2.1 m telescope (f/7.5) at the Observatorio Astronómico Nacional, San Pedro Mártir, B. C., México on 1995 July 29–31, 1996 June 14–17, 1997 August 3–4, 1998, December 11–14, 1999 October 4–7, and 2000 November 1–3. The REOSC Echelle Spectrograph plus the University College London camera (described by Levine & Chakrabarty 1993) were always used. Two different CCD detectors were employed: for observations in 1995 and 1996 we used a CCD Tektronix

TABLE 1

OBSERVING LOG[a]

PN G	Usual name	Obs. dates (dd/mm/yy)
013.7 − 10.6	YC 2-32	02/11/00
037.7 − 34.5	NGC 7009	01/11/00
084.9 − 03.4	NGC 7027	02/11/00
103.7 + 00.4	M 2-52	02/11/00
104.4 − 01.6	M 2-53	01-02/11/00
118.0 − 08.6	Vy 1-1	02/11/00
130.3 − 11.7	M 1-1	01-02/11/00
133.1 − 08.6	M 1-2	01-02/11/00
147.4 − 02.3	M 1-4	03/11/00
159.0 − 15.1	IC 351	11/12/98
166.1 + 10.4	IC 2149	13/12/98
194.2 + 02.5	J 900	02/11/00
196.6 − 10.9	NGC 2022	02/11/00
215.2 − 24.2	IC 418	12-13/12/98
221.3 − 12.3	IC 2165	03/11/00
243.8 − 37.1	PRTM 1	12-13-14/12/98
294.1 + 43.6	NGC 4361	04/10/99

[a]Observing set-up: 2048×2048 ($14 \times 14\,\mu$m^2) pixel CCD detector; slit dimensions: $4'' \times 13''$, oriented E–W; wavelength range 3360–7360 Å, spectral resolution ~ 0.2 Å. Extraction window: $4'' \times 3''$, for all the objects.

of 1024×1024 (23μm) pixels, providing an average spectral resolution of 0.3 Å (about 18 km s^{-1} in velocity) with a 150μm slit width, and since 1997 we used a CCD Thomson of 2048×2048 (14μm) pixels, giving a resolution of 0.2 Å (about 11 km s^{-1}) with the same slit width.

The observations for most of WRPNe and WLPNe presented here were described in Paper II, where a detailed list of objects, observing dates, exposure times and instrumental set-up were given. In Table 1 we present the log of observations for objects not reported in Paper II (mainly WLPNe and ordinary PNe). As usual we have taken at least two consecutive observations for each object in each run. Different exposure times (from 2 to 15 minutes) were used to obtain a S/N better than 3 for the weak lines without saturating the most intense ones. The different exposures for the same object were averaged to increase the S/N. The slit was always E–W oriented. In this work, the reported data correspond always to those obtained for the central zone (the slit was centered on the central star). For all the objects we covered a wide spectral range (at least from 3700 to 6800 Å); therefore lines for high and low ionized species were obtained. This is important for studying the kinematics on different zones of the nebula where such species reside.

A Th–Ar lamp was used for wavelength calibration in all the spectral ranges and a tungsten bulb was used for flat fielding. Standard stars from the list by Hamuy et al. (1992) were observed each night for flux calibration. Data reduction was performed using the package IRAF[4] and includes standard bias-subtraction and flat-field correction for all spectra.

In Table 2, we present some nebular characteristics (diameter, electron temperatures from the [O III] lines, densities from the [S II] lines and ionic abundance ratios) for all the objects for which the kinematical analysis is performed. Most of the data was taken from Papers I and II. For the new objects (Table 1) the nebular characteristics were derived by using the same procedures as reported in those papers. In addition, in columns 8 to 11 of Table 2 we present the stellar classification, stellar temperature and wind parameters, taken from the literature. All these data will be used in the interpretation of the kinematical data.

3. LINE PROFILES

[WC] stars present intense and wide emission lines of helium, carbon, and other elements, whose wavelengths occasionally coincide with the wavelengths of some nebular lines. For instance, this is the case of the nebular He II, He I, and H Balmer lines which coincide with stellar He II and He I lines, and especially this is the case of [N II] λ6583 and [S II] λ6731 which appear on the top of some C II multiplet 2 lines. High spectral resolution is necessary to safely deblend the nebular and stellar components and to study the nebular profiles. This is important for all [WC]-type objects but it is essential for compact nebulae around [WC]-late stars where the stellar winds show terminal velocities of a few 100 km s^{-1} (see Table 2), and the stellar lines present a FWHM of a few Å. Therefore a spectral resolution better than 5000 is necessary. This is one of the advantages of our spectra (resolution of 18,000). In Appendix A, we present stellar and nebular lines for some of our objects (particularly [WC]-late type objects) to show that our spectral resolution allows us to safely deblend both components for most of the objects. Thus the nebular lines have been measured without stellar contamination.

[4]IRAF is distributed by NOAO, which is operated by AURA, Inc. under contract with the NSF.

Also, the high spectral resolution of our data allows us to obtain well resolved nebular profiles for all the sample, except for a couple of objects showing FWHM of lines smaller than our instrumental resolution. Therefore, we have an extensive data set including different kind of objects, obtained in a consistent way, which allows us to perform a reliable comparative analysis of the kinematics. First we will analyze the adequacy of deriving expansion velocities from the line profiles.

3.1. *Line Profiles and Velocity Field*

A nebular line profile depends on several internal properties such as the nebular morphology, the density distribution, the thermal and ionization structures, the turbulence, the expansion velocity, etc. In addition, the observed profile also depends upon the spectral resolution and the position and dimensions of the slit: for instance, when the nebula is extended and the slit just covers the central zone, the classical double-peak profile is obtained. Many authors have derived the nebular expansion velocity, $V_{\rm exp}$, as half the separation of the peaks. On the other hand, when the slit includes the entire nebula, or when we are dealing with a filled nebula (with a very small inner hole, as could be the case of a very young nebula) a single profile is usually observed. In such a case, the half width at half maximum (HWHM) has been used to measure $V_{\rm exp}$. In our sample, many nebulae do not present a well defined shell, or they have knots at different velocities, showing then complex profiles, for which is difficult to derive $V_{\rm exp}$ in a straightforward manner.

An ad-hoc detailed kinematical model, including the density distribution (3D-morphology) and the ionization and thermal structuctures of the nebula, would be required to deconvolve the effect of each contribution to the line profile. An approach to this procedure, using a spherically symmetric model, can be found in Gesicki, Acker, & Szczerba (1996), Gesicki, Acker, & Zijlstra (2003), and other papers by the same authors. More recently, tomography techniques or 3D spatio-kinematic models have been used to calculate the line profiles of some individual nebulae (Sabbadin et al.2004 and references therein; Monteiro et al. 2005). The main weaknesses of such a procedure are that the results are strongly model dependent, the derived model is probably not unique, and it is very time consuming.

It is beyond the scope of this work to develop such a model for each of our objects. Our main aim is to derive reliable expansion velocities for different ions (which, due to the ionization structure, are located at different distances from the central star) to compare the behavior of WRPNe with those of non-WRPNe and to address, if possible, the effects due to turbulence.

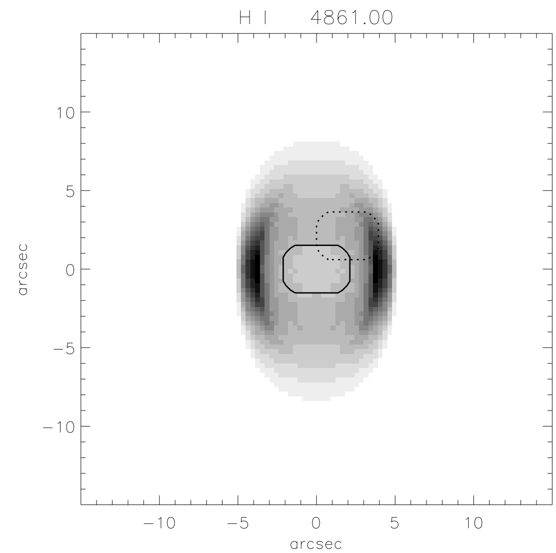

Fig. 1. The Hβ surface brightness of the modeled nebula is shown. Two slits of $3'' \times 4''$ centered and off-center are superimposed. They are used to produce "observed profiles" (see § 3.1).

To relate the line profiles with the values of the real expansion velocities for our objects in a consistent manner, we have used the code NEBU-3D, presented by Morisset, Stasińska, & Peña (2005), to compute a spatio-kinematic model for analyzing the line profile behavior of a simple and common case: an ellipsoidal nebula ionized by a central star with an effective temperature of 80,000 K and a luminosity of 10^{35} erg s^{-1}. The chemical abundances are solar. The nebula has an internal elliptical hole with the major axis twice the minor axis. The orientation of the polar axis makes an angle of 45° with the line of sight (thus the nebula is in between "polar-on" and "face on" orientations). The density is constant in the radial direction, but varying with the polar angle according to $\rm N(H)_{inner} = N(H_0) \times (R_0/R_{inner})^2$, where $\rm N(H_0)$ and R_0 are the hydrogen density and the inner radius at the equator. The dependence of N(H) with the polar angle is included in the parameter R_{inner} which follows the ellipsoidal form.

Figure 1 presents the Hβ surface flux distribution, projected on the sky. The nebular dimensions projected on the sky are about $5'' \times 7''$ (a distance of 1.87 kpc is assumed). Two "observing slits" (a $3'' \times 4''$ slit, centered, and a similar one, off-center) have been superposed. These slits are used to extract "observational" data to compare with our own.

TABLE 2

NEBULAR AND STELLAR PHYSICAL PARAMETERS[a]

PN G	Name	T_e (10^4 K)	N_e (cm^{-3})	$\mathrm{He}^{++}/\mathrm{He}^{+}$	$\mathrm{O}^{++}/\mathrm{O}^{+}$	ϕ (arcsec)	[WC][b]	T_* (10^3 K)	v_∞ ($\mathrm{km\,s^{-1}}$)	log $\dot{M}$ ($M_\odot\,\mathrm{yr}^{-1}$)	Ref.
001.5 − 06.7	SwSt 1	1.06	30000	0.0	0.3	5	9	40	900	−6.72	dM01
002.4 + 05.8	NGC 6369	1.01	3220	0.1	15.7	38	4	150	1200	−6.15	KH97a
002.2 − 09.4	Cn 1-5	1.09	4700	0.0	82.8	7	4	< 57	···	···	TS94
003.1 + 02.9	Hb 4	0.96	4600	0.1	33.9	7.2	3−4	86	···	···	TS94
004.9 + 04.9	M 1-25	0.80	10400	0.0	43.6	3.2	6	60	···	···	L96
006.8 + 04.1	M 3-15	0.87	7443	0.0	38.8	4.5	5	55	···	···	ZK93
011.9 + 04.2	M 1-32	0.99	6720	0.0	12.1	9	4−5	66	···	···	TS94
012.2 + 04.9	PM 1-188	0.94	200	0.0	0.03	4	10	35	360	−5.70	LH98
017.9 − 04.8	M 3-30	1.03	525	0.9	27.2	20	2	97	···	···	TS94
027.6 + 04.2	M 2-43	1.05	10100	0.0	14.3	1.5	8	65	850	−6.08	LH98
029.2 − 05.9	NGC 6751	1.12	2730	0.0	5.2	20.5	4	135	1600	−6.12	KH97b
048.7 + 01.9	He 2-429	0.77	6810	0.0	3.6	4.2	4−5	···	···	···	
061.4 − 09.5	NGC 6905	1.21	1530	2.9	58.6	40	2−3	141	1800	−6.32	KH97a
064.7 + 05.0	BD+30°3639	1.01	21200	0.0	0.0	7.7	9	47	700	−4.87	L96
068.3 − 02.7	He 2-459	2.00:	17400	0.0	···	1.3	8	77	1000	−5.01	L97
089.0 + 00.3	NGC 7026	0.92	3250	0.2	14.7	20	3	130	3500	−6.34	KH97a
096.3 + 02.3	K 3-61	0.89	1690	0.0	···	6.1	4−5	···	···	···	
120.0 + 09.8	NGC 40	1.00	1980	0.0	0.1	48	8	78	1000	−5.62	L96
130.2 + 01.3	IC 1747	1.12	2380	0.2	78.6	13	4	126	1800	−6.58	KH97a
144.5 + 06.5	NGC 1501	1.05	1020	0.7	···	52	4	135	1800	−6.28	KH97a
146.7 + 07.6	M 4-18	0.86	6350	···	0.0	3.7	10	31	160	−6.05	dMC99
161.2 − 14.8	IC 2003	1.28	3840	1.38	21.4	8.6	3	88	···	···	TS94
243.3 − 01.0	NGC 2452	1.30	1590	0.7	6.0	19	2	141	3000	−6.20	KH97a
352.9 + 11.4	K 2-16	1.17	504	···	0.4	13.5	11	30	300	−6.36	L97b
009.4 − 05.0	NGC 6629	0.84	3470	0.0	13.5	15.5	wl	< 52	···	···	TS94
010.8 − 01.8	NGC 6578	0.79	2270	0.0	240	8.5	wl	65	···	···	TS94
011.7 − 00.6	NGC 6567	0.95	4360	0.01	28.3	7.6	wl	61	1950	···	TS94
096.4 + 29.9	NGC 6543	0.79	5640	0.0	75.4	19.5	wl	< 66	1900	−7.4	TS94
100.6 − 05.4	IC 5217	1.12	8850	0.1	93.9	6.6	wl	72	···	···	TS94
159.0 − 15.1	IC 351	1.31	2500	1.0	24.7	7	wl	85	···	···	TS94
194.2 + 02.5	J 900	1.13	1110	0.7	9.2	9	wl	123	···	···	TS94
221.3 − 12.3	IC 2165	1.41	3984	0.8	19.0	9	wl	153	···	···	TS94
356.2 − 04.4	Cn 2-1	0.97	5320	0.07	74.2	2.4	wl	84	···	···	P-M91
013.7 − 10.6	YC 2-32	0.88	3337	0.03	···	15	pn	68	···	···	TS94
037.7 − 34.5	NGC 7009	1.08	4371	0.3	151.8	28.5	pn	85	2750	−8.55	TS94
084.9 − 03.4	NGC 7027	1.64	30000	1.1	2.8	14	pn	175	···	···	TS94
103.7 + 00.4	M 2-52	1.41	879	1.3	127.1	14	pn	···	···	···	
104.4 − 01.6	M 2-53	1.11	496	0.1	1.6	14.8	pn	112	···	···	TS94
118.0 − 08.6	Vy 1-1	0.99	2101	0.0	56.6	5.2	pn	32	···	···	TS94
130.3 − 11.7	M 1-1	2.7:	3000	46.7	7.2	6	pn	87	···	···	TS94
133.1 − 08.6	M 1-2	···	4264	0.02	···	18	pn	51	···	···	TS94
147.4 − 02.3	M 1-4	1.03	6276	0.06	···	4	pn	67	···	···	TS94
166.1 + 10.4	IC 2149	0.95	10000	0.0	6.8	8.5	pn	< 49	1290	−7.7	TS94
196.6 − 10.9	NGC 2022	1.51	800	8.7	62.5	19	pn	114	···	···	TS94
215.2 − 24.2	IC 418	0.87	18000	> 0.1	0.44	12	pn	53	1050	−8.2	TS94
243.8 − 37.1	PRTM 1	1.63	1200	7.8	> 300	23	pn	90	···	···	P90
294.1 + 43.6	NGC 4361	1.93	800	> 19	> 180	63	pn	95	···	···	TS94

[a]Nebular data are mostly from Paper II. Nebular diameter ϕ is from Acker et al. 1992. T_*, v_∞ and log $\dot{M}$ values were taken from literature, and the references are: dM01: De Marco et al. (2001); dMC99: De Marco & Crowther (1999); KH97a: Koesterke & Hamann (1997a); KH97b: Koesterke & Hamann (1997b); L96: Leuenhagen et al. (1996); L97a: Leuenhagen (1997a), L97b: Leuenhagen (1997b); LH98: Leuenhagen & Hamann (1998); P90: Peña et al. (1990); P-M91: Preite-Martinez et al. (1991); TS94: Tylenda & Stasińska (1994); ZK93: Zhang & Kwok (1993).
[b]Central star type is as following: a number indicates the [WC] spectral type, *wl* is for WELS and *pn* for normal stars.

The expansion velocity of the modeled nebula grows with the distance from the star as V = 60 R/R_{max} km s^{-1} (R_{max} = 4.2 10^{17} cm is the distance from the central star to the pole). A turbulent component of 0.5 km s^{-1} has been added to the expansion.

We consider that this hypothetical nebula represents adequately the majority of nebulae. We have verified that for other morphologies (like spherical or bipolar nebulae) the results do not differ significantly from the conclusions presented here. A very simple spherical case has been analyzed by Gesicki & Zijlstra (2000) providing very similar results. An extensive sample of elliptical and bipolar objects seen in different orientations and with different conditions will be presented in a catalog of profiles to be published elsewhere (Morisset et al., in preparation).

The main characteristics of our modeled nebula are presented in Figure 2. The upper panels show the density, temperature and velocity structures as function of the distance from the central star (in units of R_{max}) along the equator (solid lines) and along the polar axis (dotted lines). The second row of panels presents the surface brightnesses computed for Hβ, He II λ4686, and [N II] λ6583, as a function of the distance from the central star along the same directions. The third row of panels presents the line profiles of Hβ, He II λ4686, and [N II] λ6583 as a function of the velocity, obtained by integrating through the two slits shown in Fig. 1. The solid lines present the profiles through the centered slit (this slit has the same size and position as our extraction window), while the dotted lines show the profile through the off-center slit. The lowest row of panels shows the profiles through a $30'' \times 30''$ slit which includes the whole nebula. Superposed to these profiles we have traced horizontal lines indicating the values of $V_{\rm exp}$ as measured with different methods: the heavy solid line is the "real velocity", computed as the average velocity of the ion weighted by the emissivity of the line, the thin solid line is the peak-to-peak velocity, the dotted line is the HWHM velocity and the dashed line is the velocity at 1/10 the maximum intensity of the profile (V_{10}, see § 5).

The main results of our model, as it is observed in Fig. 2, show that when the nebula is well centered in the slit and it is fully resolved (third row of panels) it presents symmetric double-peak profiles and that half the peak-to peak separation is a very good approach for the "real velocity", underestimating it by less than 10%.

The HWHM of the profile overestimates the "real velocity" by about 10%. The profiles obtained when the slit is off-center (dotted profiles) are always asymmetrical and it is very difficult to measure the expansion velocities from them, as the separation between peaks is smaller than the centered case.

When the nebula is fully included in the slit, it presents single Gaussian profiles and the HWHM of the profiles is a good measurement of the expansion velocity within 20%. As expected due to the adopted velocity law, [N II] λ6583 presents a higher expansion velocity than He II λ4686, and Hβ, and the latter one shows much wider lines due to the thermal broadening (which is included).

V_{10} is always larger than the 'real velocity' by about 30–40%, but it is closer to the velocity of the most external (although faint) zones and it is useful to detect high-velocity low-emission components in the gas.

3.2. *Our Observed Profiles*

The line profiles obtained for our objects fall mainly into five different categories: (a) symmetric double-peak profiles found mainly in extended objects, (b) single Gaussian-type profiles usually found for compact symmetrical nebulae, the prototype being M 4-18 whose [N II]λ6583 profile is shown in Figure 3a, (c) single asymmetrical profiles as seen in Fig. 3b, usually produced by asymmetric nebulae (or produced by aspherical nebulae where the slit did not cross exactly the center), (d) single profiles with wide wings or 'shoulders' as shown in Fig. 3c (this could be due to high velocity gas or highly turbulent gas; high velocity components have been reported for some objects, e.g., De Marco, Barlow, & Storey 1997), (e) complex profiles showing several components which usually correspond to knotty nebulae as the one presented in Fig. 3d.

For the first two categories, $V_{\rm exp}$ can be measured safely in the classical form: from half the peak-to-peak separation for the well-resolved objects and from the HWHM for objects showing single lines with no asymmetries nor complex profiles. Our measurements are presented in the next section. Objects with very asymmetrical profiles, for which it is very difficult to define the expansion velocity in a simple way, were excluded from the $V_{\rm exp}$ analysis. For all the objects, the type of line profile is indicated in the last column of Table 5.

For the kinematical analysis, the profiles of Hβ, He II λ4686, [O III] λ5007, and [N II] λ6583 lines were measured when available. The purpose for selecting these lines was to study possible kinematical differences between lines arising from ions located at different distances from the central star. For instance, while the Hβ line is mapping the whole nebula, He II λ4686 and [O III] λ5007 lines give information about the inner and intermediate regions, and [N II] λ6583 gives information about the outer regions.

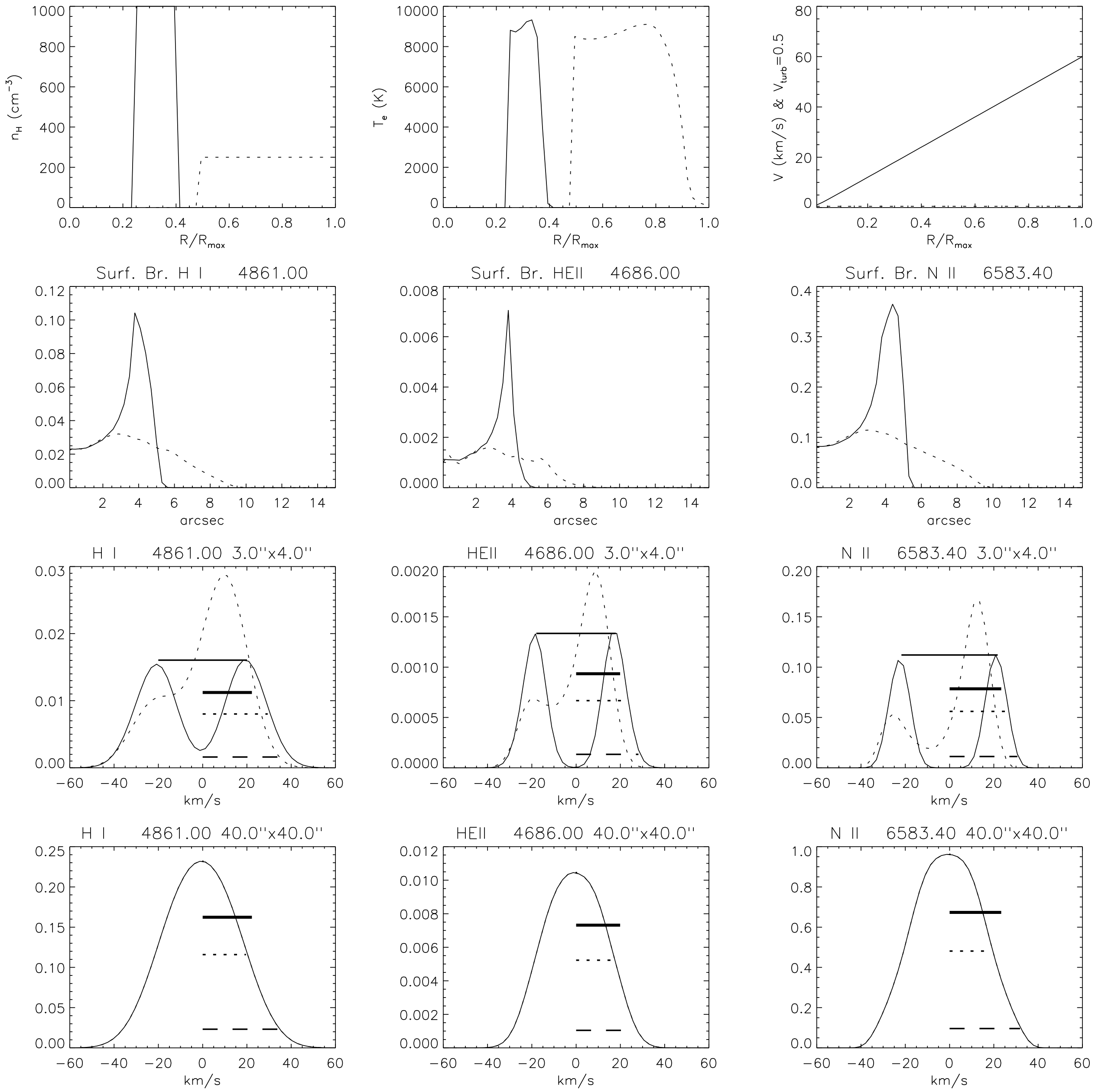

Fig. 2. Upper panels show the density, temperature and velocity distributions in the modeled nebula. The second row of panels shows the surface brightness along the equator (solid lines) and the polar axis (dotted lines) for several emission lines. The third row of panels shows the line profiles obtained through the centered slit (solid lines) and the off-center slit (dotted profile). The horizontal lines represent the "real velocity" (heavy solid line), the peak-to-peak (thin solid line), the HWHM (dotted line) and V_{10} (dashed line) velocities, for the centered slit. The lowest panels show the line profiles through a slit of $30'' \times 30''$, including the whole nebula.

4. EXPANSION VELOCITIES

4.1. *Objects with Split Profiles*

Twelve objects of our sample (six WRPNe, two WLPNe, and four ordinary PNe) present symmetrical split profiles. Remember that according to our model such profiles are observed for well resolved nebulae and half the peak-to-peak separation is a good approach for $V_{\rm exp}$. Values for [O III] λ5007, Hβ, [N II] λ6583, and He II λ4686 lines are presented in Table 3. Typical errors are ± 5 km s^{-1}. The [WC] type of the central stars or an indication if the star is a WELS or a "normal" central star is listed in Col. 3.

The line widths (FWHM) for each component of Hβ, ΔV_1, and ΔV_2 (in km s^{-1}), are also listed. The instrumental and thermal widths have been subtracted from each line width by assuming that they add in quadrature. The instrumental widths were measured from the comparison lamp lines (using the same slit widths as in the observations) and they turned out to be 18 km s^{-1} for observations prior to 1997 (23μ pixel size CCD) and 12 km s^{-1} for those since 1997 (14μ pixel size CCD). The thermal contribution to line width for any ion can be expressed as $\Delta V_{\rm th} = 21.4\sqrt{t_{\rm e}/A}$ (km s^{-1}), where $t_{\rm e}$ is the electron temperature in units of 10^4 K and A is the atomic mass (Lang 1980); therefore for Hβ, $\Delta V_{\rm th} = 21.4\sqrt{t_{\rm e}}$ while for [O III], $\Delta V_{\rm th} = 5.35\sqrt{t_{\rm e}}$, etc. The electron temperature employed for each object has been listed in Table 2.

The individual line widths in Table 3, in the range of 18–30 km s^{-1}, are therefore mainly due to turbulence and possible velocity gradients within the shell. In this sense notice that the model presented in § 3, which has a velocity gradient producing $\Delta V \geq 20$ km s^{-1} from side to side of the shell, predicts a FWHM of about 5–6 km s^{-1}for the double-peak profiles (third row of panels in Fig. 2), after subtracting the thermal width. Our objects in Table 3 present much higher ΔV, possibly produced by turbulence.

Table 3 (see also § 6.1) shows that, for a given object, the expansion velocities from different ions are, in general, very similar, although most of the objects have slightly larger $V_{\rm exp}$([N II]) than $V_{\rm exp}$([O III]) or $V_{\rm exp}$(Hβ) which, as in our model, might be indicating that the expansion velocity increases with the distance from the central star. This fact, predicted by hydrodynamical models as due to acceleration of the external nebular material, was already noticed by Wilson (1950) for his sample of PNe.

Our $V_{\rm exp}$ values are equal, within uncertainties, to those from the catalogue by Weinberger (1989), which have been included in Col. 10 of Table 3. In Col. 11 we have also included the expansion velocities found by Acker et al. (2002), based upon modeling the velocity field, for the few objects in common; their $V_{\rm exp}$ values and ours coincide, except for the faint and extended WRPN K 2-16 for which Acker et al. give two different values. A deeper analysis of K 2-16 is found in the Appendix B.5.

For the sample presented in Table 3, we found that WRPNe have $V_{\rm exp}$ values (as measured from [O III] lines) ranging from 24 to 44 km s^{-1} with an average of 36 km s^{-1}, while WLPNe and ordinary PNe show $V_{\rm exp}$ from 17 to 26 km s^{-1} with an average of 21.5 km s^{-1}. That is $<V_{\rm exp}({\rm WRPNe})>$ is 67% larger than $<V_{\rm exp}({\rm non\text{-}WRPNe})>$. Therefore, definitely, WRPNe in this sample have larger expansion velocities than non-WRPNe (WLPNe and ordinary PNe). Also, a systematic trend of higher $V_{\rm exp}$ with earlier [WC] type seems to be present. This result will be strengthened in the following sections.

In addition to higher $V_{\rm exp}$, WRPNe seem also to show larger line widths than non-WR objects. This is particularly true for WRPNe with early [WC] stars such as NGC 6905, NGC 6369, NGC 6751, and NGC 1501, which in principle are more evolved, probably indicating large turbulence in these nebulae.

In conclusion, WRPNe with split profiles are showing higher expansion velocities and probably more turbulence than WLPNe and ordinary PNe. This does not agree with the results presented by Acker et al. (2002), who have concluded that the expansion velocities in WRPNe and non-WRPNe are similar but WRPNe are much more turbulent than non-WRPNe. In addition, their models would indicate that ordinary PNe present acceleration in the outer nebular zones, while WRPNe do not, which is not the case for our objects.

4.2. *Objects with Single Profiles*

The FWHM of [O III] λ5007, Hβ, [N II] λ6583, and He II λ4686 were measured for all the objects showing single symmetrical profiles (alternatively [N II] λ6548 was measured when the stellar C II lines were severely blended with [N II]λ6583. See Appendix A). Instrumental and thermal widths were subtracted as indicated in § 4.1. We have assumed that HWHM represents the expansion velocity plus turbulence. The results are presented in Table 4 where, in Col. 8, we have included $V_{\rm exp}$([O III]) from the compilation by Weinberger (1989) or from more recent literature, and in Col. 9, the values reported by Acker et al.(2002).

Although in this case it is more difficult to compare kinematical data measured by different authors using different procedures, it is found that the majority of our values coincides within a factor of 1.2 with those from the literature. For several objects (M 1-32, He 2-459, K 1-61, and YC 2-32), $V_{\rm exp}$ are determined for the first time.

Typical errors for our measurements are ±6–8 km s^{-1} for [N II] and He II lines and ±4 km s^{-1} for [O III] and Hβ lines. We have searched for systematic

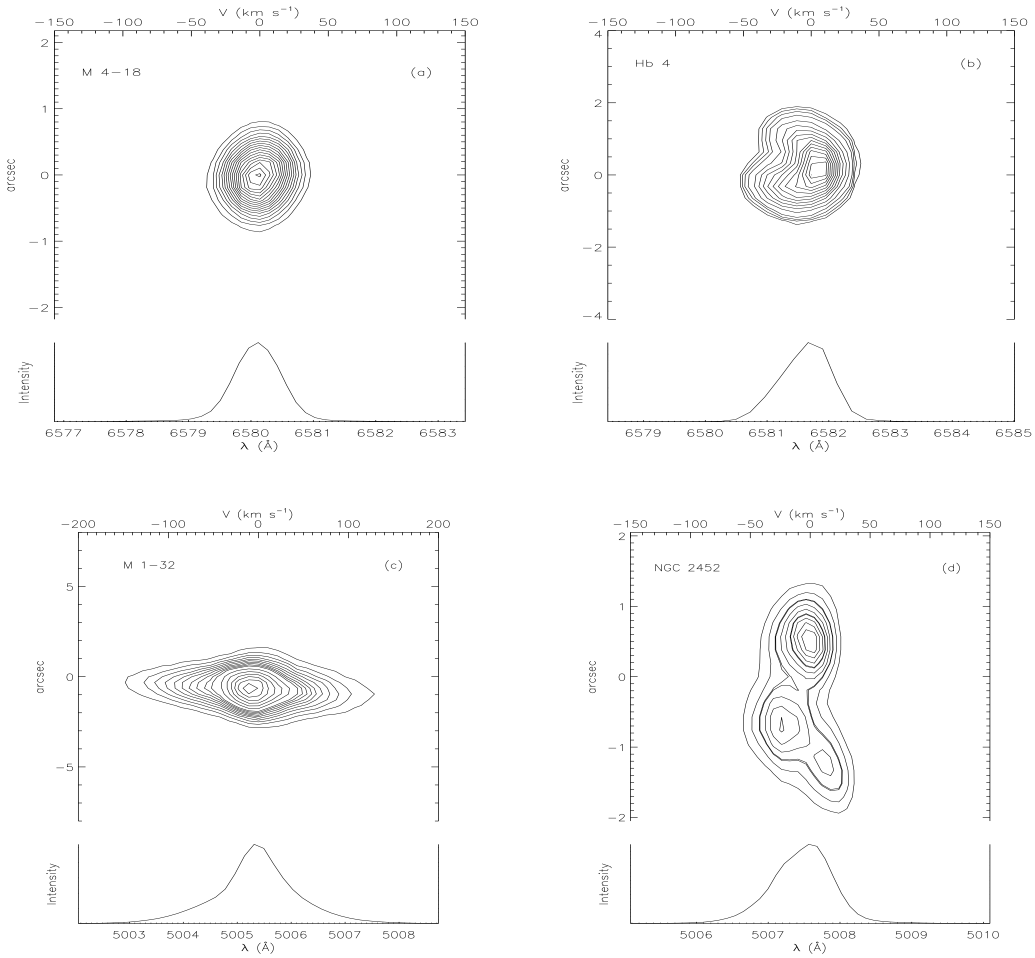

Fig. 3. Position-velocity diagrams and integrated profiles from the extracted spectra are shown featuring the different types of line profiles found in our sample. The different types are: (a) simple Gaussian [N II] λ6583 profile of M 4-18, (b) asymmetrical [N II] λ6583 profile of Hb 4, (c) [O III] λ5007 high velocity wings found in M 1-32, (d) knotty structure and complex [O III] λ5007 profile in NGC 2452. At the top of each figure, a velocity scale helps to visualize the velocity profile. The 0 corresponds to the maximum line intensity.

errors (as, e.g., a dependence of $V_{\rm exp}$ as a function of electron temperatures) and found that these errors appear to be negligible. Also, possible contamination of nebular lines with stellar emission lines, producing artificial broadening of nebular lines, is discarded as a source of important systematic errors (see Appendix A). Systematic trends of $V_{\rm exp}$ with electron density and stellar temperature are found for all the sample but these are real trends and they are discussed in the following sections.

$V_{\rm exp}$ averages of the 14 WRPNe in Table 4 are 23, 23, and 25 km s^{-1}, for [O III], Hβ and [N II], respectively. The corresponding averages for the 5 WLPNe are 19, 18, and 22 and for the ordinary PNe they are: 19, 17, and 20. WLPNe and ordinary PNe show a very similar behavior and can be put together in a single sample, non-WRPNe, showing averages of 19, 18, and 20 km s^{-1} for [O III], Hβ, and [N II]. Therefore, the averages for WRPNe are 20–25% larger than the corresponding averages for non-WRPNe indicating that WRPNe have wider lines. In this case we cannot disentangle expansion velocities from turbulence, but this result is consistent with the results found in § 4.1 of higher expansion velocities and probably higher turbulence in WRPNe than in non-WRPNe.

As in the case of double-peak objects, here the $V_{\rm exp}$ average for [N II] is about 2 km s^{-1} larger than the corresponding values for [O III], regardless of whether they are WRPNe or non-WRPNe, confirming that the external shells might be expanding faster in all kinds of nebulae.

TABLE 3

EXPANSION VELOCITIES AND TURBULENCE FOR NEBULAE WITH DOUBLE PEAK LINES

PN G	Name	[WC][a]	$V_{\rm exp}$ (km s^{-1})[b]				ΔV_1[b]	ΔV_2[b]	$V_{\rm exp}$(OIII)[c]	$V_{\rm exp}$[c]
			[O III]	Hβ	[N II]	He II	Hβ	Hβ	W89	A02
061.4 − 09.5	NGC 6905	2-3	44	41	46	40	25	17	44	···
002.4 + 05.8	NGC 6369	4	36	36	37	38	24	38	42	···
029.2 − 05.9	NGC 6751	4	42	40	40	···	24	29	40	41
144.5 + 06.5	NGC 1501	4	40	40	42	38	20	19	37	40
120.0 + 09.8	NGC 40	8	30	26	26	···	18	< 15	29	···
352.9 + 11.4	K 2-16	11	24	24	26	···	22	16	···	34 or 38
100.6 − 05.4	IC 5217	wl	18	18	23	18	16	20	23	···
011.7 − 00.6	NGC 6567	wl	17	18	27	···	< 20	< 20	19	···
037.7 − 34.5	NGC 7009	pn	20	18	21	16	< 15	< 15	21	···
196.6 − 10.9	NGC 2022	pn	24	21	21	23	16	20	27	···
243.8 − 37.1	PRTM 1	pn	24	23	···	23	28	26	···	···
294.1 + 43.6	NGC 4361	pn	26	22	···	22	32	20	21	···

[a]Central star type as in Table 2.

[b]Uncertainties: ± 5 km s^{-1} for $V_{\rm exp}$, and ± 8 km s^{-1} for line widths. ΔVs were corrected for thermal and instrumental widths.

[c]References are: W89: Weinberger (1989); A02: Acker et al. (2002).

5. LINE WIDTHS AT THE BASE OF LINES

Considering that an important fraction of PNe shows kinematical features like ansae, BRETS, FLIERS, jets, high velocity ejecta, etc., (see Balick & Adam 2002 for a complete list and definition of these terms), all of them produced by non-spherical, bipolar, multipolar or asymmetrical ejections of the central star, it seems likely to expect some additional perturbations in the velocity field of WRPNe as compared with non-WRPNe, caused by the high mass-loss [WC] wind. For instance, the hydrodynamical computations of García-Segura & McLow (1995) have shown that the expansion of a hot bubble pushed by a WR wind results in a filamentary broken shell with probably large turbulence.

Therefore, in order to perform a comparative kinematical analysis of all our sample, including all these effects, we have decided to consider the nebular gas showing the highest velocity relative to the central star. This can only be measured at the base of the line profiles (half the full width at zero intensity). To avoid any noise disturbance due to the low signal at the base of the lines, we measured such a velocity as half the width of the line profile at one tenth maximum intensity (V_{10}), after subtracting the instrumental and thermal widths as described in § 3.1. A similar treatment was previously used by Dopita et al. (1985) to determine expansion velocities of a sample of planetary nebulae in the SMC.

To carry out a systematic treatment of all the observed data, V_{10} was determined for all the objects, including those cases where a single Gaussian adequately reproduced the shape of the lines or when the line profile showed a double peak (objects in Tables 3 and 4). In the latter case, half the full width at 1/10 intensity of each component was added to the peak-to-peak separation. It can be easily calculated that, for a single Gaussian profile, half the full width at 1/10 I max can be expressed as:

$$V_{10} = 0.911 \text{ FWHM} \quad (\mathrm{km\,s^{-1}})\,;$$

while for double peak profiles (two Gaussians), it is found that:

$$V_{10} = V_{\rm exp} + 0.455\,(\Delta V_1 + \Delta V_2) \quad (\mathrm{km\,s^{-1}})\,.$$

We have used these expressions to derive V_{10} for our objects in Tables 3 and 4. For non-Gaussian, wing-extended, or complex profiles, V_{10} was measured directly from the line profiles.

V_{10} derived in such a way includes not only the expansion velocity of the shell, but also the turbulence of the gas and faint high velocity components, if they exist. The values are listed in Table 5. Uncertainties are about ± 5 km s^{-1} and larger if marked with a colon. In the last column of Table 5 we describe the line profiles: s for single, d for double peak, c for complex, and h for high velocity components. The kinematics presented by our objects, as derived from $V_{\rm exp}$ and V_{10}, is discussed in detail in the next section.

6. KINEMATICAL ANALYSIS

In previous works, several authors have searched for correlations among the nebular velocity field and the nebular and stellar parameters. The reported results are not always consistent. For instance, Sabbadin (1984) and others have reported a correlation between the nebular radius and $V_{\rm exp}$, which has been interpreted as changes in $V_{\rm exp}$ as a consequence of nebular evolution. Gesicki & Zijlstra (2000) have not found such a correlation for a sample of bulge PNe with well determined distances. Also, as said before, acceleration of the external nebular shells (appearing as larger $V_{\rm exp}$ for low ionization species like N^+ and O^+, than for O^{++}) seems to be a well established fact for the majority of PNe. Nevertheless, from their kinematical model, Acker et al. (2002) reported no evidence of such an acceleration for WRPNe, but recently Gesicki et al. (2003) —using a similar model for a sample of 14 PNe— found that the line profiles of most nebulae in their sample can be better reproduced by adopting an U-shape velocity field (velocities in the inner and outer nebular zones appear larger than the velocity in the middle), whether the central star is of the [WC] type or not.

In this section we use our consistent data to compare the behaviour of $V_{\rm exp}$ with several properties of the nebulae and their central stars, searching the physical causes affecting the velocity field in WRPNe.

6.1. $V_{\rm exp}$ *from Different Ions*

In Figure 4, the values of $V_{\rm exp}$ derived from [N II], He II, and [O III] lines are plotted against the value derived from Hβ (data from Tables 3 and 4). Different kinds of objects (WRPNe, WLPNe, and PNe) are shown with different symbols and typical error bars are presented in each graph (± 8 km s^{-1} for [N II] and He II, and ± 4 km s^{-1} for [O III] and Hβ). An immediate result from this figure is that $V_{\rm exp}$ for WRPNe extends over a wide range from 10 km s^{-1} up to 50 km s^{-1}, while $V_{\rm exp}$ for ordinary PNe and WLPNe are always lower than 30 km s^{-1}. For the whole sample, the averages of $V_{\rm exp}$ for WRPNe are about 40–45% larger than the averages found for non-WRPNe. Notice that, as already said in § 4, $\langle V_{\rm exp}({\rm WRPNe})\rangle / \langle V_{\rm exp}(\text{non-WRPNe})\rangle$ is larger for double-peak objects than for objects with single profiles —a figure clearly showing this phenomenon was presented in our Paper II (see Fig. 2 in that paper). As double peak nebulae are more extended and

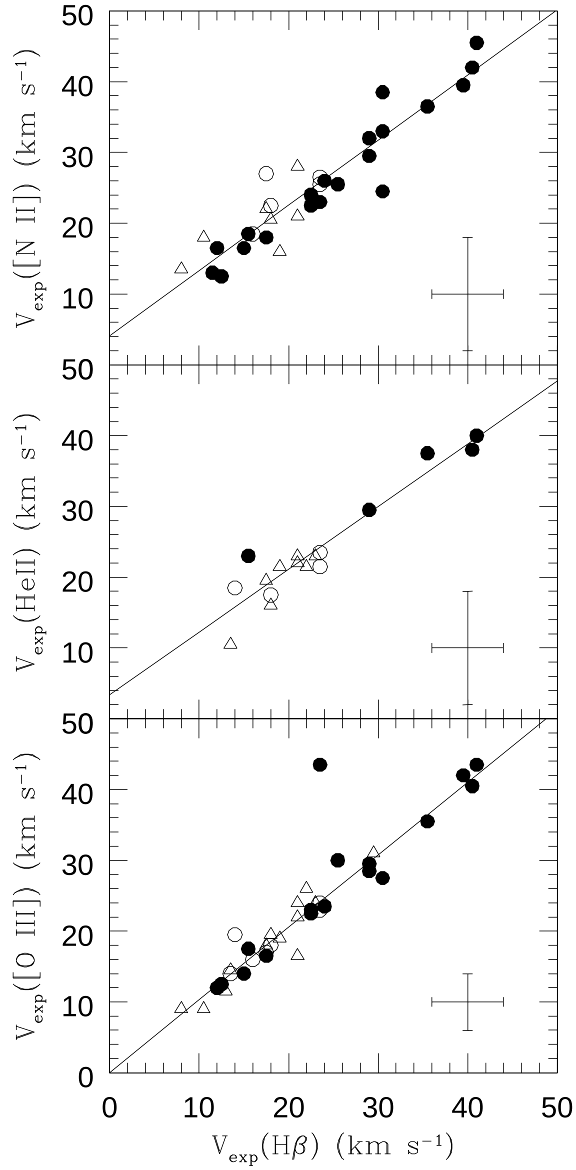

Fig. 4. $V_{\rm exp}$ from Hβ are compared to $V_{\rm exp}$ from: [N II], He II, and [O III]. WRPNe are marked with black circles, WLPNe are marked with open circles and ordinary PNe are marked with open triangles. Least squares fits are shown as solid lines. Typical error bars are shown in each case. The WRPN conspicuously away from the $V_{\rm exp}$([O III]) versus $V_{\rm exp}$(Hβ) relation is BD+30°3639 which is discussed in Appendix B.

TABLE 4

EXPANSION VELOCITIES IN OBJECTS WITH SINGLE SYMMETRICAL LINES

PN G	Main Name	[WC][a]	$V_{\rm exp}$ (km s^{-1})[b]				$V_{\rm exp}$[c]	$V_{\rm exp}$[d]
			[O III]	Hβ	[N II]	He II	[O III]	
			λ5007	λ4861	λ6583	λ4686	W89	A02
001.5 − 06.7	SwSt 1	9	12	12	17	···	13[1]	17
002.2 − 09.4	Cn 1-5	4	23	22	24	···	18:	···
004.9 + 04.9	M 1-25	6	23	23	23	···	···	30
006.8 + 04.1	M 3-15	5	17	17	18	···	···	16
011.9 + 04.2	M 1-32	4-5	≤ 13	≤ 13	≤ 13	···	···	···
012.2 + 04.9	PM 1-188	10	···	30	38	···	···	···
027.6 + 04.2	M 2-43	8	14	15	17	···	···	20
048.7 + 01.9	He 2-429	4-5	28	29	32	···	···	···
064.7 + 05.0	BD+30°3639	9	43	23	23	···	(e)	28
068.3 − 02.7	He 2-459	8	···	32	33	···	···	···
096.3 + 02.3	K 3-61	4-5	28	32	25	···	···	···
130.2 + 01.3	IC 1747	4	30	29	30	30	28	···
146.7 + 07.6	M 4-18	10	···	12	13	···	19[2]	15
010.8 − 01.8	NGC 6578	wl	16	16	19	···	···	···
159.0 − 15.1	IC 351	wl	20	14	16:	19	15	···
194.2 + 02.5	J 900	wl	23	24	27	22	13	···
221.3 − 12.3	IC 2165	wl	24	24	26	24	20	···
356.2 − 04.4	Cn 2-1	wl	14	14	···	18:	23[3]	···
013.7 − 10.6	YC 2-32	pn	18	18	22	20	···	···
084.9 − 03.4	NGC 7027	pn	22	21	28	22	22	···
103.7 + 00.4	M 2-52	pn	19	19	16	22	8	···
104.4 − 01.6	M 2-53	pn	17	21	20:	22:	11	···
118.0 − 08.6	Vy 1-1	pn	12	13	18:	···	10	···
130.3 − 11.7	M1-1	pn	31	30	22:	···	39	···
147.4 − 02.3	M 1-4	pn	15	14	···	11	14	···
166.1 + 10.4	IC 2149	pn	< 9	11	18	···	< 10	···
215.2 − 24.2	IC 418	pn	< 9	8	14	···	< 6	15

[a]Central star type as in Table 2.

[b]Typical errors are ±6–8 km s^{-1} for [N II] and He II, and ±4 km s^{-1} for Hβ, and [O III]. Errors are larger for the cases marked with a colon.

[c]Data are from Weinberger (1989) unless indicated otherwise. Other references are: 1: De Marco et al. (2001); 2: De Marco & Crowther (1999); 3: Gesicki & Zijlstra (2000).

[d]A02: Acker et al. (2002).

[e] Bryce & Mellema (1999) reported $V_{\rm exp}$([O III])=36, $V_{\rm exp}$([N II])=28 km s^{-1} for BD+30°3639.

presumably older objects this would indicate that evolved WRPNe expand faster that evolved non-WRPNe. This indication will be strengthened in the following sections.

Fig. 4 shows that $V_{\rm exp}$ for [N II], He II, and O III follow a very close 45° linear correlation with

TABLE 5

V_{10} FOR THE SELECTED IONS

PN G	Usual Name	[WC][a]	V_{10} (km s^{-1})[b]						Profiles[c]
			[O II] λ3729	[O III] λ5007	Hβ λ4861	[N II] λ6583	He I λ5876	He II λ4686	
001.5 − 06.7	SwSt 1	9	29	22	22	30	···	···	s
002.4 + 05.8	NGC 6369	4	76:	64	64	57	67	63:	d,c
002.2 − 09.4	Cn 1-5	4	46	42	41	44	···	···	s
003.1 + 02.9	Hb 4	3-4	47:	32	32	34	31	42	s,a
004.9 + 04.9	M 1-25	6	36	41	41	41	43	···	s
006.8 + 04.1	M 3-15	5	···	30	32	29	36	···	s,h
011.9 + 04.2	M 1-32	4-5	63	89	62	65	76	···	s,h
012.2 + 04.9	PM 1-188	10	···	···	56	70	···	···	s
017.9 − 04.8	M 3-30	2	41:	52	49	68	49	52	c
027.6 + 04.2	M 2-43	8	26	26	27	30	30	···	s
029.2 − 05.9	NGC 6751	4	64	66	63	60:	81:	···	d
048.7 + 01.9	He 2-429	4-5	···	52	54	59	···	···	s
061.4 − 09.5	NGC 6905	2-3	64	64	60	64	68	67	d
064.7 + 05.0	BD+30°3639	9	62	79	43	42	···	···	s
068.3 − 02.7	He 2-459	8	···	···	56	60	···	···	s
089.0 + 00.3	NGC 7026	3	68	54	55	62	59	52	d,c
096.3 + 02.3	K 3-61	4-5	···	48	57	46	51	···	s
120.0 + 09.8	NGC 40	8	37:	47	38	36	40	···	d
130.2 + 01.3	IC 1747	4	25:	55	54	58	55	56	s,a
144.5 + 06.5	NGC 1501	4	···	58	54	51	61	66	d
146.7 + 07.6	M 4-18	10	24	···	21	24	···	···	s
161.2 − 14.8	IC 2003	3	40	42	39	44	···	···	c
243.3 − 01.0	NGC 2452	2	40:	56	58	55:	57	60:	c
352.9 + 11.4	K 2-16	11	50:	44	42	48	···	···	d
009.4 − 05.0	NGC 6629	wl	34	25	30	···	31	···	c
010.8 − 01.8	NGC 6578	wl	32	29	30	34	···	···	s
011.7 − 00.6	NGC 6567	wl	38	35	34	···	···	···	d
096.4 + 29.9	NGC 6543	wl	43	34	33	43	33	···	c
100.6 − 05.4	IC 5217	wl	62:	34	34	62	34	25	d
159.0 − 15.1	IC 351	wl	35	36	26	28:	34	34	s
194.2 + 02.5	J 900	wl	···	42	43	49	48	39	s
221.3 − 12.3	IC 2165	wl	47	44	43	47	44	43	s
356.2 − 04.4	Cn 2-1	wl	28	26	25	34:	29:	32:	s
013.7 − 10.6	YC 2-32	pn	···	33	32	40	34	36	s
037.7 − 34.5	NGC 7009	pn	36	33	30	38	33	29	d
084.9 − 03.4	NGC 7027	pn	53	40	38	51	44	40	s
103.7 + 00.4	M 2-52	pn	32	35	35	32	33	39	s
104.4 − 01.6	M 2-53	pn	36	30	37	36:	39	39:	s,a
118.0 − 08.6	Vy 1-1	pn	36:	21	24	32:	26	···	s
130.3 − 11.7	M 1-1	pn	36:	57	54	38:	57	···	s
133.1 − 08.6	M 1-2	pn	···	48	42	57::	41	49	c
147.4 − 02.3	M 1-4	pn	···	27	25	54:	34	19	c
166.1 + 10.4	IC 2149	pn	32	< 18	20	33	26	···	c
196.6 − 10.9	NGC 2022	pn	···	40	37	38	47	49	d
215.2 − 24.2	IC 418	pn	19	< 18	15	25	21	···	s
243.8 − 37.1	PRTM 1	pn	···	48	50	···	···	47	d
294.1 + 43.6	NGC 4361	pn	···	50	46	···	···	52	d

[a]Central star type as in Table 2.
[b]Uncertainties of V_{10} values are in average about of 4-5 km s^{-1}, and larger for the cases marked with a colon.
[c]Line profiles are as following: s : single compact, a : asymmetrical, h : high velocity extensions, d : double peak, and c : complex.

$V_{\rm exp}$(Hβ), although in the case of [O III] versus Hβ there is one WRPN, BD+30°3639, that conspicuously departs from this behavior. This object is discussed in more detailed in Appendix B. Interestingly, we do not find significant differences among WRPNe, WLPNe, and PNe; all kinds of objects present the same correlations within the uncertainties. The least squares fits shown in Fig. 4 are:

- $V_{\rm exp}([\mathrm{N\,II}]) = (0.92 \pm 0.08)\, V_{\rm exp}(\mathrm{H}\beta) + (4.0 \pm 2.0)$,
  $r = 0.94$,

- $V_{\rm exp}(\mathrm{He\,II}) = (0.89 \pm 0.12)\, V_{\rm exp}(\mathrm{H}\beta) + (3.0 \pm 2.9)$,
  $r = 0.95$,

- $V_{\rm exp}([\mathrm{O\,III}]) = (1.02 \pm 0.08)\, V_{\rm exp}(\mathrm{H}\beta) + (0.0 \pm 2.0)$,
  $r = 0.98$.

From Fig. 4 and from the least squares fits it can be seen that the [N II] versus Hβ correlation shows a larger dispersion but, within the errors, it is indicating that on average, $V_{\rm exp}$([N II]) is slightly larger than $V_{\rm exp}$(Hβ). [He II] versus Hβ correlation also might indicate that $\langle V_{\rm exp}(\mathrm{He\,II})\rangle$ is slightly larger than $\langle V_{\rm exp}(\mathrm{H}\beta)\rangle$ but the uncertainties are larger in this graph and the result is not conclusive. On the other hand, $V_{\rm exp}$([O III]) is equal, within the uncertainties, to $V_{\rm exp}$(Hβ). As already said, higher $V_{\rm exp}$ for low ionization species have been found in other PN samples (Wilson 1950; Gesicki et al. 2003), and could be due to acceleration of the external zones relative to the inner nebular shell or to higher turbulence of the external zones due to shocks or expansion of the ionization front against the neutral external material. We found that such a phenomenon is occurring in WRPNe as well as in non-WRPNe.

The same statistical results are obtained if we use V_{10} as given in Table 5. V_{10} averages for WRPNe are also about 40–45% larger than the respective averages of non-WRPNe. As V_{10} is computed for a larger number of objects the results are strengthened. Nevertheless the main importance in the analysis of V_{10} compared to $V_{\rm exp}$ is the possible detection of very extended wings or high velocity components produced by low emission gas, which are only noticeable when V_{10} is employed. This will be discussed in more detail in the following sections.

6.2. *Correlation of $V_{\rm exp}$ with the Nebular Density*

In Figure 5 (top), nebular electron densities derived from the [S II] line ratio are plotted versus $V_{\rm exp}$ from Hβ. The graph has a large scatter. A wide range of velocities corresponds to a given density, but it is evident that, regardless of the stellar type (WR or not) there is no object with low density showing a small $V_{\rm exp}$. That is, the nebular density and $V_{\rm exp}$ are anti-correlated. It should be remembered that high density PNe are considered young nebulae; therefore the behavior found in Fig. 5 (top) is confirming an evolutionary effect in the sense that low density

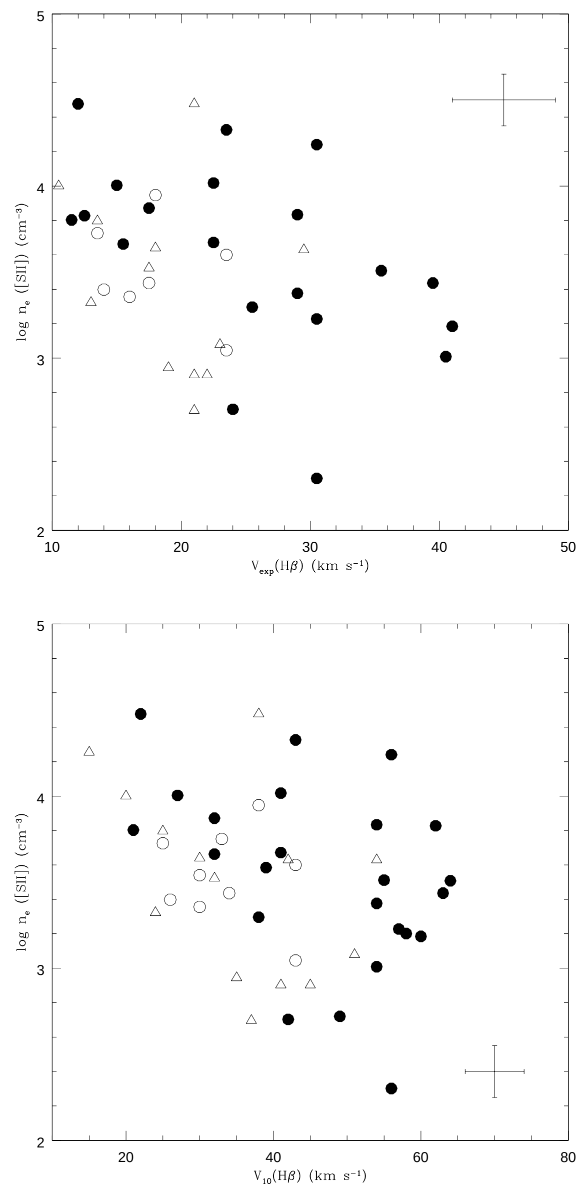

Fig. 5. Electron densities derived from [S II] line ratio are plotted versus $V_{\rm exp}$ (top) and V_{10} (bottom) from Hβ. Symbols are as described in Fig. 4. Despite the large scatter, both quantities are anticorrelated. The upper open triangle at log n$_e$=4.48 in both panels, corresponds to the young PN NGC 7027.

(therefore evolved) nebulae expand faster and possibly have larger turbulence than high density (young) objects.

In this figure, young high-density WRPNe (all of them ionized by [WC]-late stars), present a wide range in velocities (from 12 to 30 km s^{-1}) while most young ordinary PNe and WLPNe are constrained to $V_{\rm exp} \leq 20$ km s^{-1}. Certainly, the powerful [WC] wind seems to largely affect the velocity fields in seemingly young PNe. For the objects lying in the low density zone (log $n_e \leq 3.5$), WRPNe appear much faster than normal PNe. Our sample includes only three WLPNe in this zone, but they show the same behavior as ordinary PNe.

Fig. 5 (bottom) shows the behavior of density against V_{10}(Hβ). The velocity ranges are wider in this case, with V_{10} from 20 to 65 km s^{-1} for WRPNe, while all WLPNe and PNe, except two, show values of $V_{10} \leq 45$ km s^{-1}. In both figures, the upper open triangle at log $n_e = 4.48$, corresponds to the young PN NGC 7027 which shows an extraordinarily large $V_{\rm exp}$ for its density. It could be indicating the existence of a dense stellar wind. This was also proposed by Keyes & Aller (1990) in order to obtain an enhanced stellar radiation field shortward 130 Å, necessary to fit a photoionization model for the nebula. In recent observations of the central star, Hubeny, Heap, & Lanz (1994) have not detected such a wind; however its presence in the near past cannot be discarded.

6.3. *Correlations of $V_{\rm exp}$ with Characteristics of the Central Stars*

6.3.1. *Stellar Temperature and Nebular Expansion*

The fundamental stellar parameters of many [WC] stars have been calculated from non-LTE expanding atmosphere models by several authors (see references in Table 2). It is found that stellar temperatures, T_*, are closely related to [WC] types (e.g., Koesterke 2001). It should be noticed that T_* given by models corresponds to the temperature at the base of the dense wind (optical depth $\tau \sim 20$, e.g., Koesterke & Hamann 1997b) and these are not necessarily the temperatures of the ionizing fluxes "seen" by the nebulae. In fact there are some well documented [WC] stars where the temperature at $\tau = 2/3$ is much lower than T_* and, as a result, the planetary nebulae show a very low ionization degree. A typical case is NGC 6751 which does not present nebular He^{++} although it is ionized by a [WC 4] star of T_*=135,000 K at $\tau = 20$. Its T_* at $\tau = 2/3$ is, however, as low as 55,500 K (Koesterke & Hamann 1997b). This is very different from what occurs in ordinary optically-thick non-WRPNe, where the He II Zanstra temperature and the stellar effective temperature are similar (Tylenda & Stasińska 1994).

To study the behavior of $V_{\rm exp}$ and V_{10} as a function of T_*, we gathered the values of T_* from the literature and they are listed in Table 2. For [WC] stars which have been modeled, the model values have been adopted. For the non-modeled WRPNe

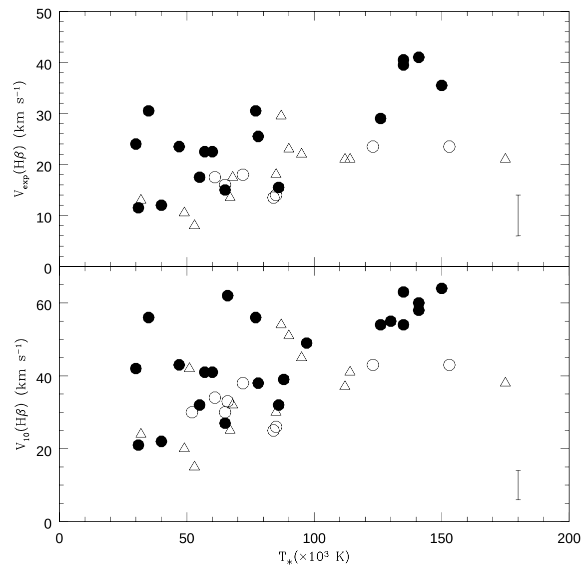

Fig. 6. $V_{\rm exp}$ (top) and V_{10} (bottom) are plotted versus the stellar temperatures. Symbols are as described in Fig. 4. Despite the large scatter, velocities and temperatures are correlated. The correlations coefficients are 0.64 for the top figure and 0.55 for the bottom figure.

and the other objects we have listed the He II Zanstra temperatures from the same data base as computed by Tylenda & Stasińska (1994). Although this is a good approximation for the effective temperature for non-WRPNe, it could be only a lower limit for the stellar temperature of [WC] stars. Thus, the Zanstra temperatures presented in Table 2 for the latter objects, in particular the [WC]-early ones, have large uncertainties that we can not determine.

Figure 6 presents the behaviour of $V_{\rm exp}$ versus T_* (top) and V_{10} versus T_* (bottom). In spite of the uncertainties affecting T_*, a clear tendency is noticed in both graphs showing that hotter central stars ionize nebulae with larger velocities and there is no object with a large T_* showing $V_{\rm exp} \leq 20$ km s^{-1}. The scatter is, however, very large and the correlation coefficients for these graphs are 0.64 for $V_{\rm exp}$ versus T_* and 0.55 for V_{10} versus T_*.

All nebulae, regardless of whether they are WRPNe or not, display this behaviour. Two main groups can be distinguished in the graphs: In the first, with T_* below 100,000 K, some WRPNe show velocities as low as non-WRPNe and both types of objects appear mixed in the lowest velocity zone; in the the second group, with $T_* \geq 100{,}000$ K, WRPNe and non-WRPNe are well separated and WRPNe fall on a zone of much higher velocities than non-WRPNe.

If it is assumed that the stellar temperature is an indicator of the age of the central star (which is the case for central stars evolving at approximately constant luminosity), then it is clear that the older the central star, the faster the nebular expansion, indicating an acceleration of the nebula with age for all type of stars. However for non-WR objects the curve in Fig. 6 seems to flatten when the stars reach $T_* \sim 100{,}000$ K. That is, non-WRPNe would stop accelerating and their $V_{\rm exp}$ reach an upper limit of about 25–30 km s^{-1} while the acceleration continues for WRPNe. Evolved WRPNe show $V_{\rm exp}$ of about 40 km s^{-1}.

This apparently continuous acceleration from young to evolved WRPNe is what one might expect if [WC] stars evolve from late to early types. A detailed hydrodynamical evolutionary model, including the kinematical effects of a long-term [WC] type wind, should be compared with the behavior detected in Fig. 6, allowing us to confirm or discard the proposed evolutionary trend. Such a model is in progress (Medina et al., in preparation) and will be published elsewhere.

The larger dispersion found in the V_{10} versus T_* graph shows that some objects, in particular some young WRPNe and also a few ordinary PNe with relatively cold stars, present large turbulence and/or high velocity components from early phases of evolution on. It results interesting that these phenomena are present in many PNe irrespective of their evolutionary age. The WRPNe M 1-32, M 3-15 and He 2-459, and the ordinary PNe M 1-1, PRTM 1 and NGC 4361 belong to this group and they are discussed in the Appendix B.

Acker et al. (2002) have not found any correlation between $V_{\rm exp}$ and T_* in their data, because they have used the stellar temperatures obtained from photoionization models. That is, they used T_* "seen" by the nebulae, which, as explained above, could be several thousands degrees lower than the temperature at the base of the wind of the [WC] star. Any possible relation is thus destroyed.

6.3.2. *[WC] Mass-Loss Rate and Wind Velocity versus Nebular Characteristics*

It is worth to notice that the kinetic energy carried by the particles in the stellar winds can easily ionize the innermost gaseous material thus perturbing the ionization equilibrium. Therefore, to analyze this possibility, in Figure 7 we present the nebular ionization degree He^{++}/He^{+} of WRPNe as a function of the mass-loss rate, $\dot{M}$, and the terminal velocity of the wind, v_∞ (all these parameters are listed in Table 2). It is evident in these graphs that highly ionized WRPNe are associated with stars with low mass-loss rates (log $\dot{M} \leq -6$) and v_∞ larger than 1800 km s^{-1}. This is expected if we consider that such wind parameters are typical of [WC]-early (therefore hot) stars, which produce very excited nebulae with large $V_{\rm exp}$. On the other hand, [WC]-late stars which have higher mass-loss rate and lower terminal velocities only produce low ionization nebulae with no traces of He^{++}. Therefore, we have found that the massive stellar winds do not contribute significantly to the ionization of nebulae and the ionization can be safely attributed to the UV stellar photons.

6.4. *The Mechanical Energy of the Stellar Wind and the Expansion Velocities*

In Figure 8 we plot $V_{\rm exp}$ as function of the rate of mechanical energy of the stellar wind, L_w, calculated as $1/2\ \dot{M}\ v_\infty^2$ with the data presented in Table 2. A very clear tendency is found showing that stars with large L_w have nebulae with large $V_{\rm exp}$. The linear fit shown has a correlation coefficient R = 0.71, indicating that, despite the scatter, the trend is real and much of the acceleration of the nebulae around [WC] stars should be due to the mechanical energy of the wind. Unfortunately only one WLPN and three ordinary PNe of our sample have published $\dot{M}$ and v_∞; nevertheless, as expected considering their low L_w, all of them lie in the low $V_{\rm exp}$ zone.

More evidence supporting this result will be discussed in a future paper, where an enlarged sample will be analyzed and a dynamical model for the evolution of the expansion velocities will be developed (Medina et al. in preparation).

7. MAIN CONCLUSIONS

Along this work we have analyzed high spectral resolution data to study and compare the kinematical behavior of a large sample of planetary nebulae around [WC] stars, as well as nebulae around WELS and ordinary PNe. The main conclusions are as follows:

- From a spatio-kinematic model representing an ellipsoidal nebula we have established that $V_{\rm exp}$ can be measured as half the peak-to-peak separation of nebular lines for well resolved nebulae observed through a centered slit. The HWHM for objects with single symmetrical profiles is also a good indicator of $V_{\rm exp}$, in particular for the cases of low turbulence.

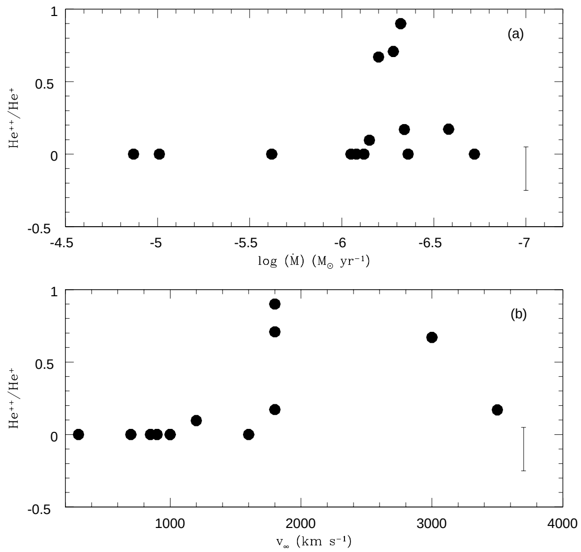

Fig. 7. Nebular ionization degree (He^{++}/He^{+}) is plotted against some stellar parameters such as: a) the mass-loss rate ($\dot{M}$), and b) the wind terminal velocity (v_∞). Symbols are as described in Fig. 4.

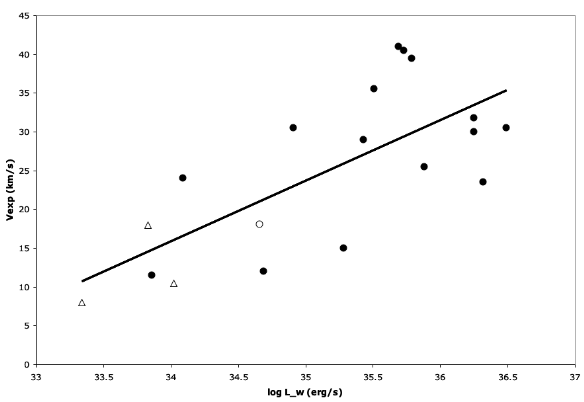

Fig. 8. $V_{\rm exp}$ is plotted against the log of the rate of mechanical energy of the stellar wind, L_w. Symbols are the same as in Fig. 4. The relation between both parameters is evident. The linear fit is $V_{\rm exp}$=7.8(log L_w) -249.3 km s^{-1}, with a correlation coefficient R = 0.71, therefore the large $V_{\rm exp}$ of WRPNe can be attributed to acceleration by the [WC] stellar wind.

- Considering the above, we measured $V_{\rm exp}$ of several ions for all the objects in our sample showing double-peak or single symmetrical profiles. For a number of objects (K 2-16, PRTM 1, M 1-32, M 2-43, He 2-429, He 2-459, K 3-61, NGC 6578, and YC 2-32) these values are presented for the first time.

- For all kinds of objects (WRPNe and non-WRPNe) it is found that the velocities of the different ions are very similar, but in general:

$$V_{\rm exp}([\rm N\,II]) \geq V_{\rm exp}([\rm O\,III]),\ V_{\rm exp}(H\beta).$$

  This indicates that all kinds of objects present acceleration of the external nebular shells.

- We have shown that WRPNe have a different kinematical behavior than non-WRPNe. For WRPNe $V_{\rm exp}$ extends over a wide range from 10 km s^{-1} up to almost 50 km s^{-1}, while the $V_{\rm exp}$ for ordinary PNe and WLPNe are always lower than 30 km s^{-1}. Average expansion velocities, measured from the peak-to-peak separation of split lines or from the FWHM of lines, are 40–45% larger in WRPNe than in non-WRPNe. This difference is larger for objects showing double-peak profiles. In addition to larger $V_{\rm exp}$, WRPNe seem to present more turbulence than ordinary PNe. These results are based mainly on our sample with double-peak profiles for which $V_{\rm exp}$ and turbulence effects are easily separated.

- It is worth to remark that PNe around WELS were found to have a velocity field very much alike the one of ordinary PNe, rather than the one of WRPNe. This evidence shows that WELS, contrary to the suggestion by Parthasarathy et al. (1998), do not belong to the [WC] family.

- To search for evidence of high velocity material and perturbations of the velocity field, the half-widths at 1/10 of maximum intensity of the nebular lines (V_{10}) were measured. We have found that $\langle V_{10}\rangle$ for WRPNe are also about 40–45% larger than the averages for non-WRPNe. But in particular V_{10} is large for some young compact WRPNe and a few ordinary PNe which would have large turbulence or high velocity material in the central zones. This phenomenon is present in many planetary nebulae irrespective of their evolutionary age.

- We found that the particles carried by the dense stellar winds, although energetic enough to ionize He^{+} and other ions, do not contribute significantly to the ionization of nebulae, and that the ionization can be safely attributed to the UV stellar photons.

- Strong evidence indicating that the nebular expansion increases with nebular age (indicated by the nebular electron density), regardless of the nebular type (WRPNe or non-WRPNe) has been found.

- The same is found when analyzing the temperature of stars: the older the central star (as measured by its temperature), the faster the nebular expansion. This behavior occurs in non-WRPNe as well, but these objects seem to accelerate to a maximum $V_{\rm exp}$ of about 25–30 km s^{-1} when their stars reach T_* of about 90,000 – 100,000 K, while WRPNe continue accelerating up to reach $V_{\rm exp}\sim$ 40 km s^{-1}. The acceleration of nebulae is closely related the mechanical energy of the stellar winds. [WC] winds accelerate more and apparently for longer time their nebulae. This constitutes an indirect evidence supporting the validity of the proposed evolutionary path: [WC]-late stars → [WC]-early stars. Another evidence for this was established years ago through the determination of the chemical abundances in [WC] stellar atmospheres. The results showed that C abundances were similar in [WC]-early and [WC]-late stars (De Marco 2002). However, these results have been recently questioned by Hamann et al. (2005) on the basis of improved non-LTE atmosphere models. These models show lower C abundance in apparently evolved [WC]-early stars than in less evolved [WC]-late ones, while one should expect the opposite. A further revision of this subject is certainly worthy.

Invaluable comments by M. Peimbert are deeply appreciated. The authors are grateful to the staff members at OAN-SPM for their technical support. This work was partially supported by DGAPA/UNAM (Grants IN114601 and IN118405), CONACYT/Mexico (Grant 32594-E), and CONACYT-CNRS Exchange Agreement. S.M. acknowledges scholarship by DGEP/UNAM and CONACYT. M.P. is grateful to DAS, University of Chile for hospitality during a sabbatical visit, supported by FONDAP-Chile and DGAPA/UNAM.

APPENDIX A

A. *Deblending Nebular from Stellar Lines*

In Figure 9 we present observed profiles of He II λ4686, He I λ5876, Hα, and [N II] $\lambda\lambda$6548,6583 lines, and [S II] $\lambda\lambda$6717,6731 for different [WC]-type objects. These lines have been chosen because some stellar lines (usually very wide) appear at the same wavelength and could affect the nebular line measurements if the spectral resolution is not adequate. These figures show that our resolution of about 18,000, allows to safely deblend the stellar and nebular lines, even in the cases of [WC]-late stars whose stellar winds show velocities of a few 100 km s^{-1} and thus their lines have FWHM of a few Å. In a few extreme cases, where [N II] λ6583 appears severely blended with the stellar C II lines, as the case of M 4-18 or NGC 40, the line width of [N II] λ6548 was measured.

APPENDIX B

B. PROFILE DESCRIPTION OF INDIVIDUAL OBJECTS

B.1. *The Peculiar M 1-32 and BD+30° 3639*

The WRPNe M 1-32 and BD+30°3639 show single symmetrical profiles, but they present V_{10} from [O III] larger than V_{10} from Hβ by about 30 km s^{-1}. For BD+30°3639 this is also the case for $V_{\rm exp}$. It is well known that this object shows this anomaly in its velocity field (Bryce & Mellema 1999 and references therein) and we have found that M 1-32 presents a similar behavior.

The spatially resolved spectroscopic study of BD+30°3639 by Bryce & Mellema (1999) shows that the N$^+$ shell is more spatially extended but less spectrally extended than the O^{++} shell. The [N II] velocity ellipses presented by these authors appear to be almost open-ended, with [O III] emission emerging from the gaps. Bryce & Mellema measured the expansion velocities from [N II] and [O III] profiles and they found 28±1 and 36±1 km s^{-1}, respectively, which coincide within the uncertainties with our values of 23 and 43 km s^{-1} for the same ions. Acker et al. (2002) reported an expansion velocity of 27 km s^{-1} with a turbulent velocity of 15 km s^{-1} for this object.

M 1-32 has very unusual profiles characterized by a very-narrow intense component (with FWHM smaller than 25 km s^{-1}) and very wide wings, with a full width at the base of about 125 km s^{-1} (see Fig. 3c). The wings are much wider in [O III] λ5007 and He I λ5876 than in Hβ and, similarly to BD+30°3639, they should be produced by high velocity gas in the unresolved central zone. Turbulence also can produce large wings, but a huge turbulence velocity should be required to create the wide wings observed (Morisset, in preparation).

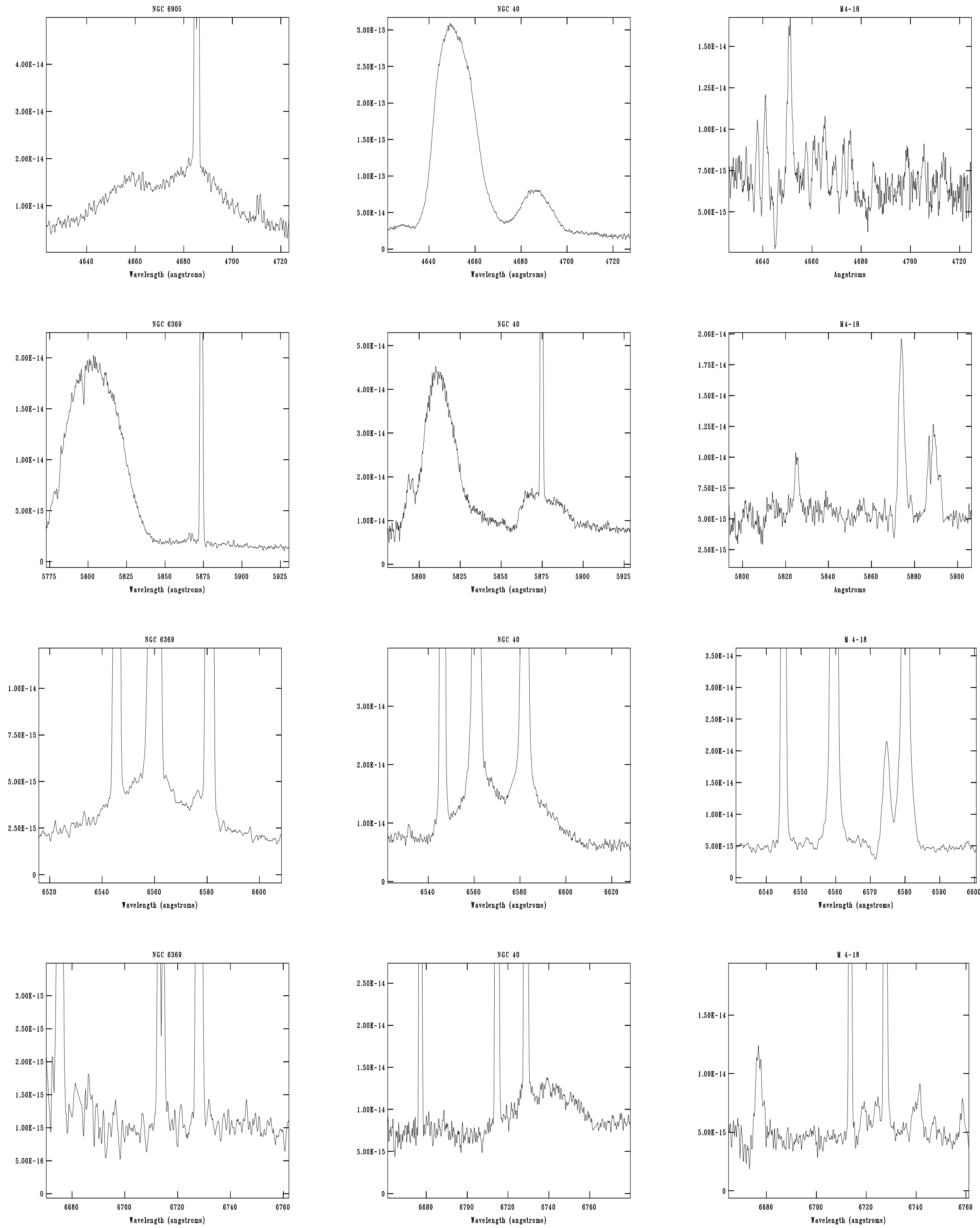

Fig. 9. Profiles of He II λ4686, He I λ5876, Hα, and [N II] $\lambda\lambda$6548,6583 lines, and [S II] $\lambda\lambda$6717,6731, showing the nebular and stellar lines for different [WC]-type objects ([WC 2-3] NGC 6905, [WC 4] NGC 6369, [WC 8] NGC 40, [WC 10] M 4-18. The nebular lines can be safely deblended from the wide stellar lines even in the cases of slow stellar winds as NGC 40 and M 4-18, except for [N II] λ6583. [N II] λ6548 can be measured instead. The latter object shows no He II neither He I nebular lines.

It should be noticed that both objects are low ionization nebulae (BD+30°3639 in particular), where O^{++} lies in the inner nebular zone which is probably interacting with (and being disturbed by) the [WC] dense and turbulent wind. It seems evident that the mechanical energy of the wind is strongly affecting the inner zone in both nebulae.

B.2. *Objects Showing Single Asymmetrical Profiles*

Fig. 3b shows the single asymmetrical line profile of [N II] λ6583 for Hb 4. This is a high excitation Type I planetary nebula with a bright central nebular core and outer low ionization structures or ansae (Corradi et al. 1996; Gonçalves et al. 2001). López, Steffen, & Meaburn (1997) showed that the ansae are produced by collimated outflows with radial velocities of ± 150 km s^{-1}, relative to the central core. They measured an expansion velocity of 21.5 km s^{-1} for the core, while the model by Acker et al. (2002) indicates expansion and turbulence velocities of 16 and 14 km s^{-1}, respectively. Our $V_{\rm exp}$ value for Hβ is 16 km s^{-1}.

Our position-velocity diagram for the central core (Fig. 3b) shows a structure similar to a broken or incomplete shell, with a bright compact knot in the red side and fainter extensions to the blue. This structure is more evident at low-ionization species and produces asymmetrical single line profiles with a V_{10} of about 32 km s^{-1}.

Another nebula with similar asymmetrical profiles is IC 1747, where we also detected a bright knot and faint extensions to the blue. Extracted profiles show an intense component with an extended blue wing. Images by Balick (1987) show a knotty ring nebula.

Among ordinary PNe, M 1-2, M 2-53, and IC 2149 show similar single asymmetrical profiles.

B.3. *Objects Showing High Velocity Extensions or Very High Turbulence*

The most conspicuous object presenting high velocity extensions is M 1-32 and was described above. Other objects showing also the same phenomenon are: He 2-459, although the profiles are not as wide as in M 1-32, and M 3-15, where two very faint high-velocity knots (located in the central zone) at -90 and 80 km s^{-1} are detected. In the latter case, the knots are faint with intensities below 0.1 $I_{\rm max}$; therefore, only the velocity of the bright component is reported in Tables 4 and 5. M 3-15 is also peculiar in the sense that this nebula shows an extraordinarily low neon abundance (Paper II).

There are three of ordinary PNe showing very large V_{10}. They are PRTM 1, NGC 4361, and M 1-1. The two first are considered halo PNe, and are both density bounded nebulae (the low ionization species, O^{+} and N^{+}, are not detected in these objects, see Peña et al. (1990) and Torres-Peimbert, Peimbert, & Peña (1990). Vázquez et al. (1999) have reported high velocity material and a complex kinematics in NGC 4361. Similarly M 1-1 shows a very high excitation with faint emission of the low ionized species. It is usual to find fast $V_{\rm exp}$ in density bounded objects (Acker et al. 2002). In these thin low-mass objects the ionization front has broken through the outer layers which apparently expand fast having no neutral material around.

B.4. *Complex (Knotty) Profiles*

Several objects having a knotty or filamentary structure show complex single profiles or several not well resolved peaks. This is the case of NGC 2452 (Fig. 3d), M 3-30, NGC 6543, IC 2003, IC 5217, M 1-2, M 1-4, and IC 2149, among others. For all these objects, only V_{10} was measured.

B.5. *K 2-16: a [WC]-Late Object with Double-Peak Profiles*

This is a very-faint extended low-ionization nebula with a shell morphology 13″ in diameter. The shell structure as well as the low electron density are unusual for a nebula around a [WC 11] star. In this sense K 2-16 is similar to the also extended and low-density PM 1-188, ionized by a [WC 10] star (Peña 2005). K 2-16 is the only nebula around a [WC]-late star showing double peak profiles. The central star is very bright (V = 12.75 mag from Acker et al. 1992) and it presents many intense emission lines severely contaminating several nebular lines, specially in the zone of [N II] λ6583 and [S II] λ6731 (higher ionized species are not detected in this nebula). Therefore we took special care in measuring the nebular lines and the expansion velocity of the nebula in a zone 4–5″ outside the stellar emission. In Figure 10 we present the extracted spectra showing "the nebular only" and "the nebular + stellar" emissions (central zone).

Our $V_{\rm exp}$ value of 24 km s^{-1} is much smaller than the expansion velocity determined by Acker et al. (2002), who proposed two models for this object: one with $V_{\rm exp}$ = 34 km s^{-1} and a turbulent velocity of 12 km s^{-1} or alternatively, a model with $V_{\rm exp}$ = 38 km s^{-1} and an acceleration producing a difference of 35 km s^{-1} between the velocities of the inner and outer radii. It seems that the stellar lines

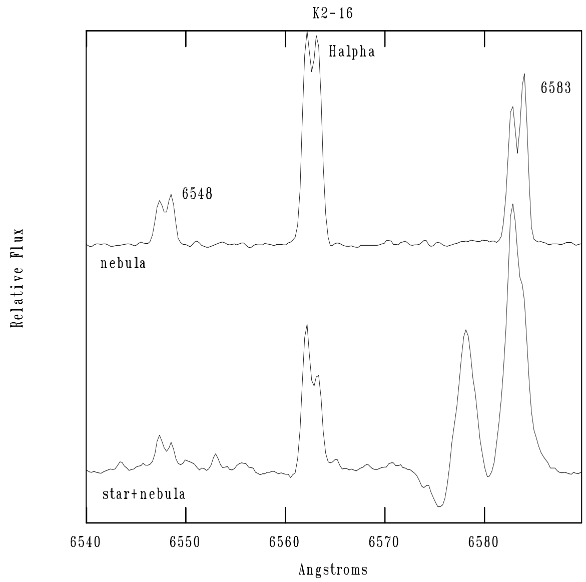

Fig. 10. Nebular only (up) and nebular + stellar (low) extracted spectra in the zone of Hα for K 2-16. The nebular spectrum was extracted at about 4-5$''$ from the central star. The nebular lines show double-peak. The stellar + nebular spectrum shows the intense stellar lines C II lines well mixed with the nebular emission, preventing to measure [N II] λ6583.

affecting the nebular [N II] λ6583 have introduced an additional uncertainty in Acker et al. model.

The kinematical behavior of K 2-16 could be explained by an old thin shell strongly accelerated by the [WC] wind of this apparently low-mass slowly-evolving star. A very simple calculation to support this idea can be made by assuming that the nebular mass of K 2-16 is about 0.1 $M_\odot$. Then the mechanical energy in the shell would be about $10^{44.76}$ erg. Thus the wind (with mechanical luminosity L_w=$10^{34.09}$ erg s^{-1} as calculated from Table 2) should have been blowing for about 1500 yr in order to provide the energy in the shell (an efficiency of a 100% is assumed). A similar calculation for M 4-18, gives an age of about 580 yr. In conclusion K 2-16 should be several times older than M 4-18, since it possesses such a low density, large diameter and high expansion velocity.

B.6. *Peculiar Line Profiles in NGC 6369*

NGC 6369 is an extended nebula with a peculiar position-velocity structure shown in Figure 11. A beautiful well resolved picture of this object is found at http://heritage.stsci.edu/2002/25/index.html. The nebula consists of a faint central zone, a very bright extended ring, and faint filamentary extensions and ansa-type structures which have been studied by Gonçalves, Corradi, & Mampaso (2001). Monteiro et al. (2004) have modeled this object as a clumpy hourglass shaped nebula. In the *HST* picture, the nebular ionization structure

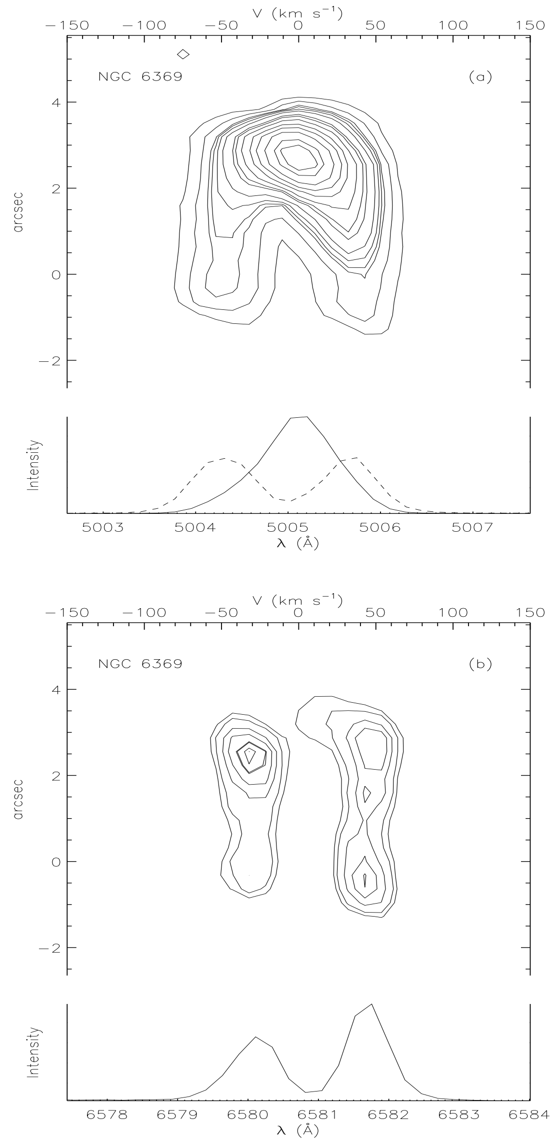

Fig. 11. Position-velocity contours and the extracted spectra from (a) [O III] λ5007 and (b) [N II] λ6583 are shown. The position of the central star is at 0$''$ in both cases. In (a), the solid line corresponds to the emission of the bright knot at 3$''$ East from the central star, whereas the dashed double-peak line corresponds to the emission at the central star position (0$''$). This emission is shown at 5$\times$ its actual intensity to feature both lines in a single plot. In (b), both emissions at 0$''$ and 3$''$ show the same split-line spectrum. The bright knot is not detected in [N II] λ6583.

can be easily seen, showing that the low ionization species are located mainly in the outer zone.

In our Fig. 11 we show that, at the low-emission central zone (0″, where the central star is located) well split lines for all the ions are detected, with $V_{\rm exp}$ of about 36 km s^{-1}. At about 3–4″ to the East from the central star we detected a very bright zone (corresponding to the inner side of the ring) emitting mainly in high excitation lines (H I, [O III], He I, and He II). These lines present single profiles. The low ionization lines ([N II], [O II], [S II] are weak in this zone and they present double peak lines. This should be the zone where Acker et al. (2002) obtained their spectrum with Hα showing a single line component and [N II] λ6583, a complex profile (see their Fig. 2). Due to the complexity of the profile in this zone they could not model this object.

REFERENCES

Acker, A., Gesicki, K., Grosdidier, Y., & Durand, S. 2002, A&A, 384, 620
Acker, A., Górny, S. K., & Cuisinier, F. 1996, A&A, 305, 944
Acker, A., Marcout, J., Ochsenbein, F., Stenholm, B., & Tylenda, R. 1992, The Strasbourg-ESO Catalogue of Galactic Planetary Nebulae
Balick, B. 1987, AJ, 94, 671
Balick, B., & Adam, F. 2002, ARA&A, 40, 439
Blöcker, T. 2001, Ap&SS, 275, 1
Bryce, M., & Mellema, G. 1999, MNRAS, 309, 731
Corradi, R. L. M., Manso, R., Mampaso, A., & Schwarz, H. E. 1996, A&A, 313, 913
De Marco, O. 2002, in IAU Symp. 209, Planetary Nebulae: Their Evolution and Role in the Universe, eds. S. Kwok, M. Dopita, & R. Sutherland, (San Francisco: ASP), 215
De Marco, O., Barlow, M. J., & Storey, P. J. 1997, MNRAS, 292, 86
De Marco, O., & Crowther, P. A. 1999, MNRAS, 306, 931
De Marco, O., Crowther, P. A., Barlow, M. J., Clayton, G. C., & de Koter, A. 2001, MNRAS, 328, 527
Dopita, M. A., Ford, H. C., Lawrence, C. J., & Webster, B. L. 1985, ApJ, 296, 390
García-Segura, G., & McLow, M.-M. 1995, ApJ, 455, 160
Gesicki, K., Acker, A., & Szczerba, R. 1996, A&A, 309, 907
Gesicki, G., Acker, A., & Zijlstra, A. A. 2003, A&A, 400, 957
Gesicki, G., & Zijlstra, A. A. 2000, A&A, 358, 1058
Gonçalves, D. R., Corradi, R. L. M., & Mampaso, A. 2001, ApJ, 547, 302
Górny, S. K., & Stasińska, G. 1995, A&A, 303, 893
Górny, S. K., Stasińska, G., Szczerba, R., & Tylenda, R. 2001, A&A, 377, 1007
Górny, S. K., & Tylenda, R. 2000, A&A, 362, 1008
Hamann, W.-R. 1997, in IAU Symp. 180, Planetary Nebulae, eds. H. Habing & H. Lamers (Kluwer), 91
Hamann, W.-R., Todt, H., & Grafener, G. 2005, AIP Conference Proceedings 804, "Planetary Nebulae as Astronomical Tools", eds. R. Szczerba, G. Stasinska, & S. Gorny, 153
Hamuy, M., Walker, A. R., Suntzeff, N. B., et al. 1992, PASP, 104, 533
Herwig, F. 2001, Ap&SS, 275, 15
Hubeny, I., Heap, S. R., & Lanz, T. 1994, A&AS, 185, 4710
Keyes, C. D., & Aller, L. H. 1990, PASP, 102, 59
Koesterke, L. 2001, Ap&SS, 275,41
Koesterke, L., & Hamann, W.-R. 1997a, in IAU Symp. 180, Planetary Nebulae, eds. H. Habing & H. Lamers (Kluwer), 114
________. 1997b, A&A, 320, 91
Lang, K. R. 1980, Astrophysical Formulae, 2nd. ed. (Springer-Verlag), 204
Leuenhagen, U. 1997a, in IAU Symp. 180, Planetary Nebula, eds. H. Habing & H. Lamers (Kluwer), 118
________. 1997b, in IAU Symp. 180, Planetary Nebula, eds. H. Habing & H. Lamers H. (Kluwer), 119
Leuenhagen, U., & Hamann, W.-R. 1998, A&A, 330, 265
Leuenhagen, U., Hamann, W.-R., & Jeffery, C. S. 1996, A&A, 312, 167
Levine, S., & Chakrabarty, D. 1993, Technical Report MU-94-04, Instituto de Astronomía, Universidad Nacional Autónoma de México
López, J. A., Steffen, W., & Meaburn, J. 1997, ApJ, 485, 697
Monteiro, H., Schwarz, H. E., Gruenwald, R., Guenthner, K., & Heathcote, S. 2005, ApJ, 620, 321
Monteiro, H., Schwarz, H. E., Gruenwald, R., & Heathcote, S. 2004, ApJ, 609, 194
Morgan, D. H., Parker, Q. A, & Cohen, M. 2003, MNRAS, 346, 719
Morisset, C., Stasinska, G., & Peña, M. 2005, MNRAS, 360, 499
Parthasarathy, M., Acker, A., & Stenholm, B. 1998, A&A, 329, L9
Peña, M. 2005, RevMexAA, 41, 423
Peña, M., Ruiz, M. T., Torres-Peimbert, S., & Maza, J. 1990, A&A 237, 454
Peña, M., Stasińska, G., & Medina, S. 2001, A&A, 367, 983 (Paper II)
Peña, M., Stasińska, G., Esteban, C., Koesterke, L., et al. 1998, A&A, 337, 866 (Paper I)
Preite-Martinez, A., Acker, A., Koeppen, J., & Stenholm, B. 1991, A&AS, 88, 121
Sabbadin, F. 1984, A&AS, 58, 273
Sabbadin, F., Turatto, M., Cappellaro, E., Benetti, S., & Ragazzoni, R., 2004, A&A. 416, 955
Torres-Peimbert, S., Peimbert, M., & Peña, M. 1990, A&A, 233, 540
Tylenda, R., Acker, A., & Stenholm, B. 1993, A&AS, 102, 595
Tylenda, R., & Stasińska, G. 1994, A&A, 288, 897
Vázquez, R., López, J. A., Miranda, L. F., Torrelles, J. M., & Meaburn, J. 1999, MNRAS,
Weinberger, R. 1989, A&AS, 78, 301
Wilson, O. C. 1950, ApJ, 111, 279
Zhang, C. Y., & Kwok, S. 1993, ApJS, 88, 137

Selene Medina, Christophe Morisset, and Mirian Peña: Instituto de Astronomía, UNAM, Apdo. Postal 70-264, 04510 México, D. F., México (miriam, morisset, selene@astroscu.unam.mx).
Grażyna Stasińska: LUTH, Observatoire de Meudon, 5, place Jules Janssen, 92195 Meudon Cedex, France (grazyna.stasinska@obspm.fr).